

Final Technical Report Award #G12AP20023

Liquefaction Hazard in Western Washington

Daniel Lavallée
Earth Research Institute
6718 Ellison Hall
UCSB
Santa Barbara, CA 93106-1100
Tel: 805-893-8467
Fax: 805-893-2578; Email: daniel@eri.ucsb.edu

Sandra H. Seale
Earth Research Institute
6708 Ellison Hall
UCSB
Santa Barbara, CA 93106-1100
Tel: 805-893-8543
Fax: 805-893-2578; Email: sandy@eri.ucsb.edu

January 1, 2012 – June 30, 2013

Abstract:

Risk associated with liquefaction caused by earthquakes requires a better understanding of the coupling between pore pressure time histories and ground motion time histories. This can be best achieved by investigating the coupling as a function of the frequency content of the seismic signals. The 2010 El Mayor-Cucapah (Baja California) earthquake (M 7.2) provides a remarkable opportunity to undertake such an investigation. The event was well recorded at the NEES@UCSB Wildlife station located 110 km from the hypocenter. The station is equipped with three-component strong-motion accelerometers at the surface and in boreholes at various depths and with pore pressure transducers located in a saturated, liquefiable layer. The recorded pore pressure and ground motion time histories are both characterized by a frequency content that is a function of time. Due to this property, investigation of the seismic signals is best achieved by using two complementary wavelet-derived tools. The wavelet correlation quantifies the degree of linear (or quasi-linear) dependence between the two signal wavelet coefficients as a function of the frequency. The square norm ratio measures the relative contribution of the wavelet coefficients to the signals as a function of the frequency and identifies the dominant wavelet coefficients necessary to reconstruct the signal. The wavelet-derived correlations are computed by matching different pairs of seismic signals, including ground motion derived velocity and displacement. A major finding of this study is the observation of a range of frequencies where wavelet coefficients of pore pressure are relatively well correlated to the wavelet coefficients of the vertical component of the velocity while the estimated square norm ratios of both wavelet coefficients follow a similar unimodal curve in the frequency domain. Results of this study may provide the basis to model the coupling between the pore pressure and the ground motion.

REPORT

1. INTRODUCTION

Pore pressure built up during an earthquake and the hazard associated with soil liquefaction present a major challenge for our society, as was dramatically displayed during the 2011 Higashi Nihon Daishinsai (Tohoku-oki, Japan) earthquake. Liquefaction is capable of causing considerable damage (e.g., Seed and Idriss, 1971; Wang and Manga, 2010). The causative mechanism responsible for liquefaction is mainly earthquake-related and is “invariability associated with high pore-water pressure.” (Wang and Manga, 2010; p. 7).

Peak ground acceleration (PGA) is the primary parameter used by geotechnical engineers to estimate hazard associated with liquefaction (Seed and Idriss, 1971). Holzer *et al.* (2009) discuss the computation of liquefaction probability curves that are conditioned on PGA and earthquake magnitude. Other parameters and mechanisms have also been discussed in the literature.

Midoriwaka and Wakamatsu (1988) found a stronger correlation between liquefaction and the peak ground velocity (PGV) rather than PGA. This lead Kostadinov and Towhata (2002) to use PGV as a parameter to identify liquefaction in earthquake records. Wong and Wang (2007) reached a similar conclusion using data generated during the 1999 Chi-Chi earthquake. Computation of the correlation between various ground motion metrics and occurrence of liquefaction and ground water level change indicates a higher correlation between low-frequency motion metrics and occurrence of liquefaction and ground water level change. Wang and Manga (2010, p. 24) concur that the “liquefaction may be more sensitive to the low frequency components of the ground motions”.

To account for the pore pressure fluctuations recorded during the 1980 Mammoth Lakes, California, earthquake, Mavko and Harp (1984) developed a first-order model relating the pore pressure to the ground motion. Their model is based on the assumptions of elastic wave propagation coupled to the hypothesis that saturated sediments can be approximated by a linear elastic solid. During the *S*-wave arrivals, the model predicts a linear relationship between the pore pressure and the surface ground velocity.

During the 2001 Nisqually, Washington, earthquake, liquefaction was reported near several sites with ground motion records. At these sites, Frankel *et al.* (2002) observed substantial amplifications in the 1–20 Hz frequency band for several sites (see Figures 5 and 6 in Frankel *et al.*, 2002), and at lower frequencies at one site (see Figure 6 in Frankel *et al.*, 2002.). In Frankel *et al.* (2002), site amplifications are attributed to nonlinear effects. They also suggest a parallel between nonlinear behavior at a site and the likelihood of liquefaction.

Recently, Holzer and Youd (2007) have undertaken an investigation of the pore pressure and ground motion acceleration recorded at the USGS Wildlife Station 5210 during the 1987 Superstition Hills earthquake. They argue that although early pore pressure build-up is associated with early high frequency oscillations present in the ground motion record, liquefaction most likely resulted from late arrivals of low frequency oscillations in the ground motion (for instance Love waves). The computed shear strain time history for the 1987 earthquake is characterized by a large low frequency fluctuation late in the signal (see Figure 7 in Holzer and Youd, 2007). A similar computation is discussed in Zeghal and Elgamal (1994).

Recent investigations discussed in Wang *et al.* (2006), Wang (2007), and Wang and Manga (2010) argued that undrained consolidation could be understood as the causal mechanism

for earthquake induced liquefaction, but only for sites located in the near field. The basis for this conclusion is a comparison between the minimum energy needed for the occurrence of liquefaction and the seismic energy available at a given site. The seismic energy is approximated by the square of the PGV. Based on this calculation, there is a direct relationship between the distribution of PGV values and the occurrence of liquefaction.

Integration of the acceleration time history, to calculate the ground velocity, reduces the amount of high frequency energy in the signal. The reduction of high frequency energy is also seen in the computed shear strain illustrated in Figure 7 of Holzer and Youd (2007). Shear strain is proportional to ground displacement, which is calculated with the double integration of the acceleration time history. Thus, the overall picture portrayed in some of the papers reviewed above suggests that pore pressure fluctuations, and thus the likelihood of liquefaction, is *more sensitive to low frequency content in the seismic waves than to the high frequency content usually associated with PGA*.

In the book “Earthquakes and Water”, Wang and Manga (2010) provide a substantial review of the available literature on the dependency of liquefaction on frequency. (Note that the materials discussed above are partially based on materials discussed in this book.) Wang and Manga (2010, p. 29) summarize well the current understanding of the relationship between pore pressure data and ground motion -or parameters derived from the ground motion:

“An unresolved issue is the complex relationship between liquefaction and the frequency of seismic waves. Current results from the field and laboratories are in conflict. Future work is needed to resolve these conflicts.”

The objective of this paper is to answer the call for “future work” by proposing a wavelet-based analysis to investigate the “complex relationship” between recorded pore pressure and ground motion time histories.

2. PORE PRESSURE AND GROUND MOTION RECORDED AT THE USGS WILDLIFE STATION 5210

In this paper, the investigation is focused on ground motion and pore pressure time histories recorded during the 2010 Sierra el Mayor-Cucapah (Baja California) Mw 7.2 earthquake at the USGS Wildlife station 5210, see Figure 2.1. The station is located at 110 km from the hypocenter, as shown in Figure 2.2. The station is equipped with three-component strong-motion accelerometers at the surface and in boreholes, at various depths and with pore pressure transducers located in a saturated, liquefiable layer. Instrumentation at Wildlife station was updated in 2004; see Steidl and Seale (2010) and Youd *et al.* (2004) for additional details. Pore pressure time histories recorded during the 2010 Sierra el Mayor-Cucapah (Baja California) earthquake are unique and unprecedented in their resolution of the time-dependent variation. Pore pressure and ground motion records are illustrated in Figures 2.3 and 2.4.

USGS Wildlife Station (5210)

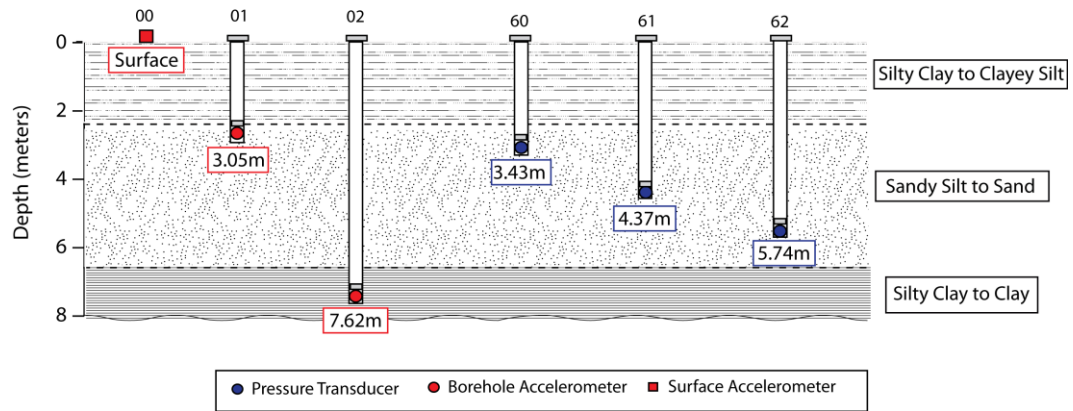


Figure 2.1: Schematic illustrations of the USGS Wildlife station (5210) showing the sediment layers and the location of the instruments. Pore pressure transducers are located at depths of 3.4 m, 4.4 m and 5.7 m with accelerometers at 0.0 m, 3.0 m and 7.6 m at the USGS Wildlife station.

This site was originally selected for its proximity to major faults and its potential for liquefaction during strong shaking. Acceleration and pore-pressure time histories from the 1987 Superstition Hills earthquake were recorded at the Wildlife station 5210. Those records (along with those from Kushiro Port, Iai *et al.*, 1995) are the basis for the current limited understanding of the complex relationship between the ground shaking and pore pressure build-up (Holzer *and al.*, 1989; Zeghal and Elgamal, 1994 and Holzer and Youd, 2007).



Figure 2.2: LIDAR image of the epicenter of the El Mayor-Cucapah event and the Wildlife Liquefaction Array.

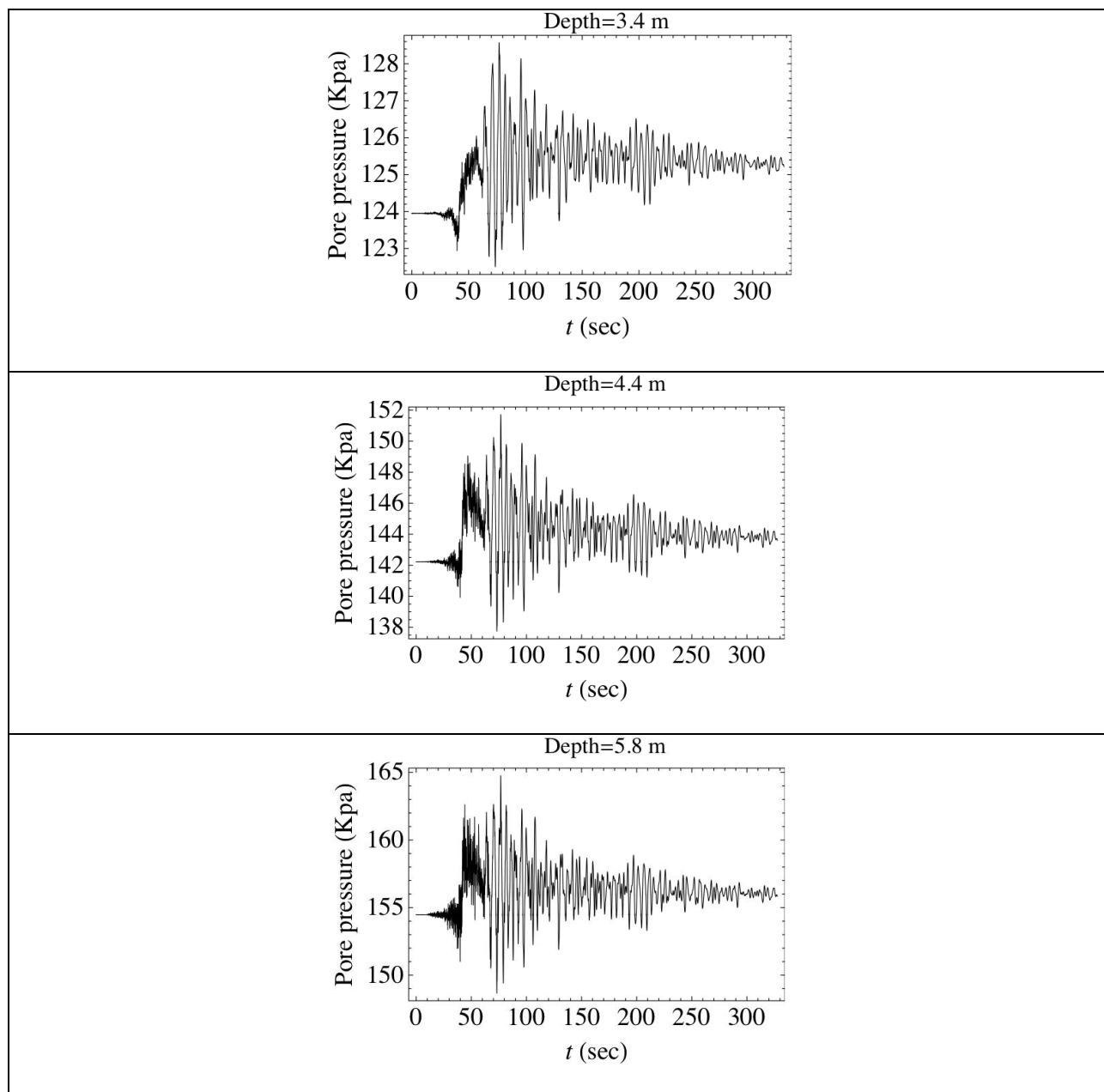


Figure 2.3: From top to bottom, pore pressure time histories recorded at different depths of the USGS Wildlife station (5210) –see Figure 1. Note that the frequency content is time dependent. More specifically, note the sharp transition in frequency content around 70 sec. Observations of high frequency waves are limited to the first 70 sec. Pore pressure is recorded at 200 Hz. In the plots above, the data are sampled at 20 Hz.

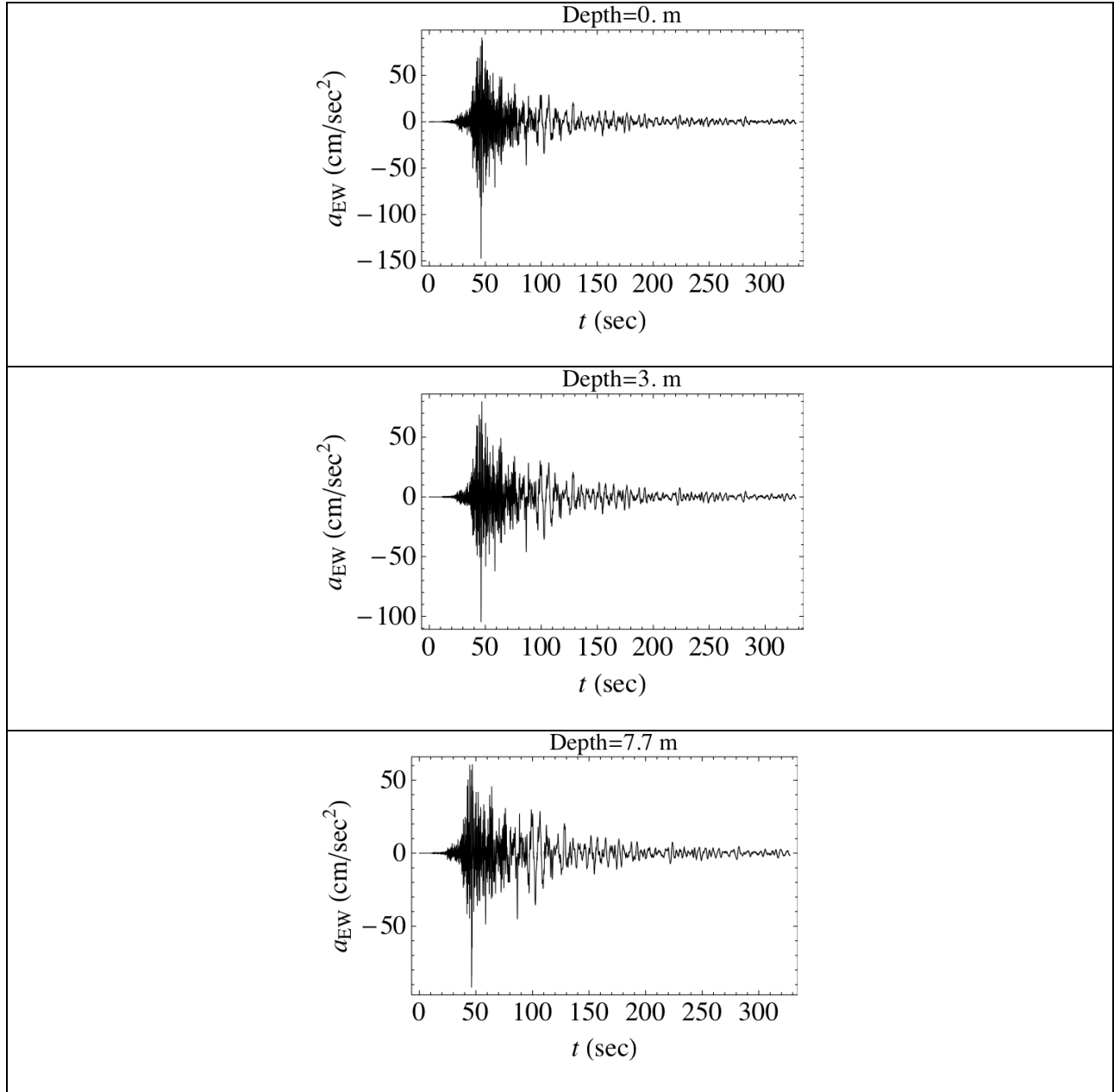


Figure 2.4: Same as Figure 2.2, except for the EW components of the acceleration time histories a_{EW} . Note that the frequency content is also time dependent, but the transition in frequency content is not as sudden as the one reported in Figure 2.3.

Accelerations at 5210 are recorded in boreholes and at the surface with Kinetmetrics Episensor Force-Balance Accelerometers. Pore pressure is recorded with ParoScientific Pressure Transducers that are installed at the bottom of the boreholes. Signals from these instruments are sampled with Quanterra Q330 digitizers at 200, 40, and 1 samples/second. The data are

transmitted through the UCSD wireless network HPWren to UCSB. The data are made available through the NEES@UCSB website at <http://nees.ucsb.edu>.

3. FOURIER ANALYSIS AND ITS LIMITATIONS

Given a pair of recorded signals, for instance ground motion and pore pressure time series, with the same causal mechanism—in our case seismic radiation—a question consists in determining the fundamental properties shared by the pair of records. Usually, investigations of the fundamental properties are done in the amplitude, time, and frequency domains. Traditional tools used to perform these investigations are often based on Fourier analysis. Due to intrinsic limitations, Fourier analysis may not be the proper tool to investigate signals characterized by transient and/or intermittent features, as explained by Mallat (1998) and Papandreou-Suppappola (2003). An illustration of transient features is given by a signal with a frequency content that gradually increases or vanishes with time, for instance the Doppler effect, as shown in examples by Riera-Guasp *et al.* (2008). Intermittent features are best exemplified by the complex time evolution of the frequency content in turbulent signals (see Chapter 4 in Addison, 2002).

Consider a signal with a distribution of frequency content that is time independent (see Figure 3.1, top). In the Fourier domain, the Fourier transform $\mathbf{F}(\nu)$ of this signal provides the distribution of frequencies included in the signal. The Fourier amplitude $|\mathbf{F}(\nu)|$, or Fourier spectrum $|\mathbf{F}(\nu)|^2$, at a given frequency ν measure the contribution of the corresponding frequency component (a sine wave) to the signal (see Figure 3.1). For a signal with a time independent frequency distribution, the relationship between the amplitude of the spectrum curve in the Fourier domain is completely and uniquely determined by the amplitude of the corresponding frequency component in the physical domain.

Alternatively, consider a signal with time varying frequency content (see Figure 3.1, center and bottom). In the Fourier domain, the frequency content is also given by the Fourier transform $\mathbf{F}(\nu)$ of the signal. However, for a signal with a time varying frequency, the Fourier amplitude $|\mathbf{F}(\nu)|$ at a given frequency ν is now a function of the amplitude and of the durations of the corresponding frequency component in the physical domain. Thus the relationship between the amplitude of the spectrum curve in the Fourier domain is neither completely nor uniquely determined by the amplitude of the corresponding frequency component in the physical domain. As pointed out in Gurley and Kareem (1999, p. 149), Fourier analysis of a signal with a time varying frequency “cannot describe the local transient features due to averaging over the duration of the signal”. The analysis and the interpretation of the distribution of frequencies in the Fourier domain is thus greatly complicated for a signal characterized by a frequency content with a transient or intermittent time dependency.

In the literature, a signal without or with time varying frequency content is sometimes referenced as a stationary or non-stationary signal (see Mallat, 1998; Goumas *et al.*, 2002; and Papandreou-Suppappola, 2003). In statistical analysis, a process is strictly stationary if its statistical properties are invariant under translation (see Papoulis, 1991). To avoid confusion between the two definitions of stationary, which are not necessary mutually exclusive, in this paper we adopt for stationary or non-stationary signals the definition used in statistics.

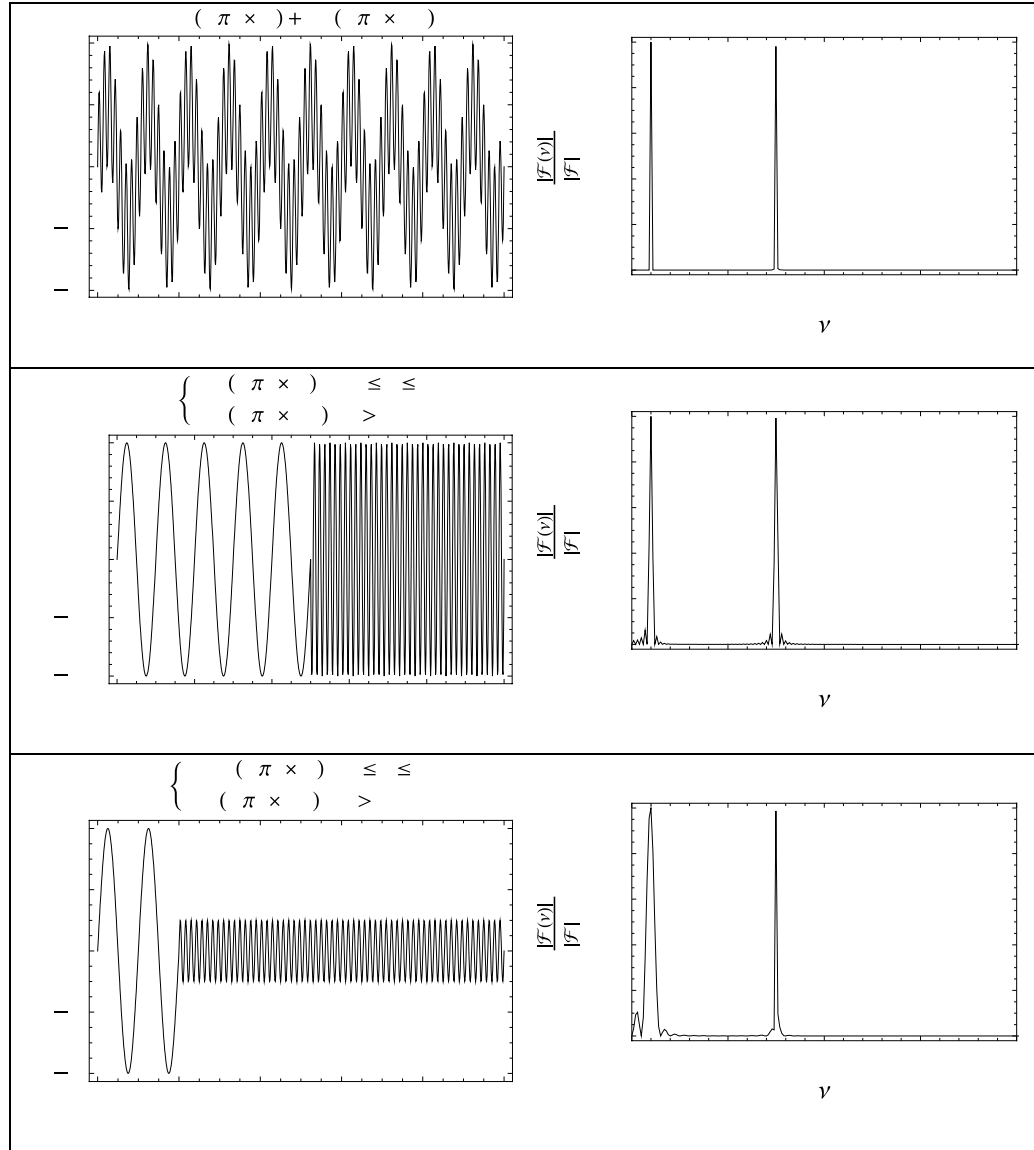


Figure 3.1: For a signal that can be understood as a sum of sinusoids, the spectrum amplitude $|F(\nu)|^2$ at a given frequency ν is uniquely determined by the amplitude of the sinusoid at the corresponding frequency in the physical domain (see top figure). This property is observed as long as the duration of all the sinusoids corresponds to the duration of the signal. When the duration of the sinusoids doesn't correspond to the duration of the amplitude, the spectrum amplitude at a given frequency depends on the sinusoid amplitude but also on the duration of the sinusoid in the time domain. The duration and amplitude dependence are both affecting the spectrum amplitude. The relationship between a sinusoid amplitude at a given frequency in the physical domain and the spectrum amplitude of the same frequency in the Fourier domain is not uniquely determined anymore. This is illustrated in the two last rows of the figure above.

Signals recorded during an earthquake are often characterized by time varying frequency content, as seen in Figures 2.3 and 2.4. Other observations of ground motion time histories with time varying frequency content are discussed in Frankel *et al.* (2002); Bonilla *et al.* (2005); and Holzer and Youd (2007). Signals with time varying frequency content recorded during aftershocks following the 3 September 2010 M 7.1 Darfield earthquake are reported in Cochran *et al.*, (2011). These observations suggest that recorded seismic signals qualified as intermittent!

The Fourier spectra of the pore pressure and East-West (EW) component of the ground motion time series recorded at 5210 during the El Mayor event are computed and illustrated in Figures 3.2 and 3.3. In all cases, the spectra are computed for a time window of 327.675 seconds and for signals recorded at different depths.

At every depth, the amplitude spectra $|F_p(\nu)|^2$ of the pore pressure p are characterized by a sharp discontinuity around 0.2 Hz. For frequencies smaller than 0.2 Hz, the spectra attenuate according to a power law. The same functional behavior is observed at higher frequencies. To capture this behavior, we assume the following relationship between $|F_p(\nu)|^2$ and the frequency ν :

$$|F_p(\nu)|^2 \propto \begin{cases} \nu^{-\eta_{\nu < 0.2}} & 0.01 \leq \nu \leq 0.1 \text{ Hz} \\ \nu^{-\eta_{\nu > 0.2}} & 0.3 \leq \nu \leq 10 \text{ Hz} \end{cases} \quad (3.1)$$

where $\eta_{\nu < 0.2}$ and $\eta_{\nu > 0.2}$ are the exponents controlling the power law decay for the frequency intervals specified in Eq. (3.1). The curves shown in Figure 3.2 are fitted with the expression given in Eq. (3.1). The computed values for the two exponents $\eta_{\nu < 0.2}$ and $\eta_{\nu > 0.2}$ are reported in Figure 3.2. As for the discontinuity observed around $\nu \gg 0.2$ Hz, there is no simple explanation for it. Future research is needed to determine the effect of the time-dependent frequency to this observation. That is, we need to investigate how much the discontinuity depends on the significant contribution of high frequency waves to the pore pressure time series during the first 70 seconds (see Figure 2.3).

For the EW acceleration components, the shapes of the amplitude spectra $|F_{a_{EW}}(\nu)|^2$ are more complicated than those reported in Figure 3.2. There is no simple functional representation of the distribution of frequency in the Fourier domain. At low frequency, the spectrum is mainly controlled by the source complexity. Note that for the EW components recorded at 3 and 7.7 m, there are depletions of the spectra at several frequencies in the range of 1 to 20 Hz. The same observations hold for the North-South (NS) components of the ground motion and to some extent to the vertical components of the ground motions. Depletions of the spectra may result from the intermittent nature of the frequency content in these frequency ranges.

To study the properties shared by two signals, one can compute the cross spectrum of the two signals. Here we consider three examples: the cross-spectrum between the pore pressure time series and each of the three components of ground motion recorded at the same depth (around 3 m depth, see Figure 3.4). The amplitude of the cross-spectrum is given by the following expression:

$$|F_p^*(\nu)F_{a_{EW}}(\nu)| \quad (3.2)$$

where $F_p^*(\nu)$ is the complex conjugate of the Fourier transform of the pore pressure time history and $F_{a_{EW}}(\nu)$ is the Fourier transform of the EW acceleration component. According to Misiti *et*

al. (2007, p. 286), “Crossed spectra, when taken as a whole, are difficult to interpret”. The cross-spectrum curves illustrated in Figures 3.4 mostly corroborate this observation.

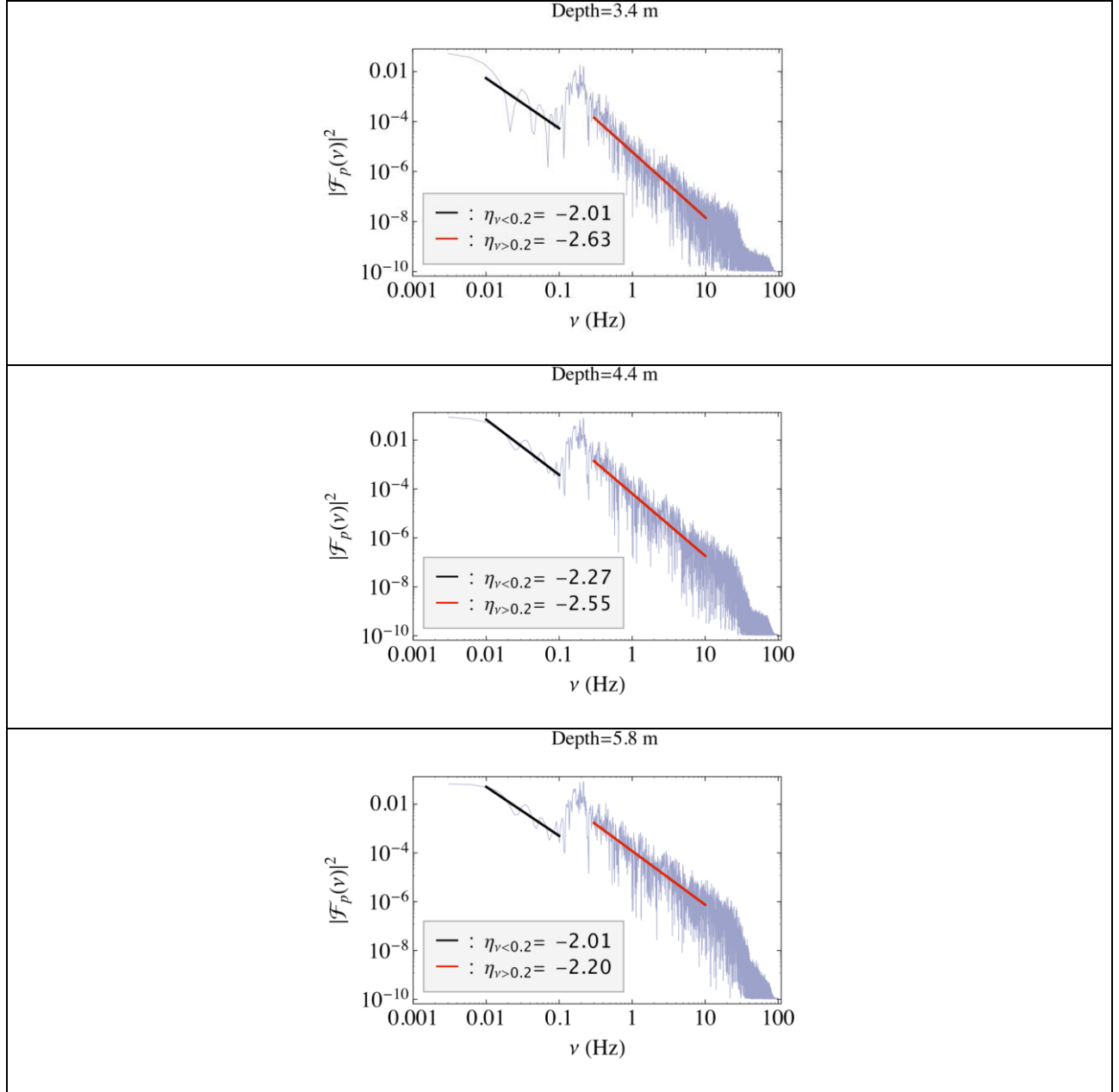


Figure 3.2: From top to bottom, the spectral curves $|\mathcal{F}_p(v)|^2$ of the pore pressure time histories p reported in Figure 2.2. The black and red straight lines represent the best fit to the expression (2.1). The values of the exponents $\eta_{v<0.2}$ and $\eta_{v>0.2}$ are reported in the left bottom corner.

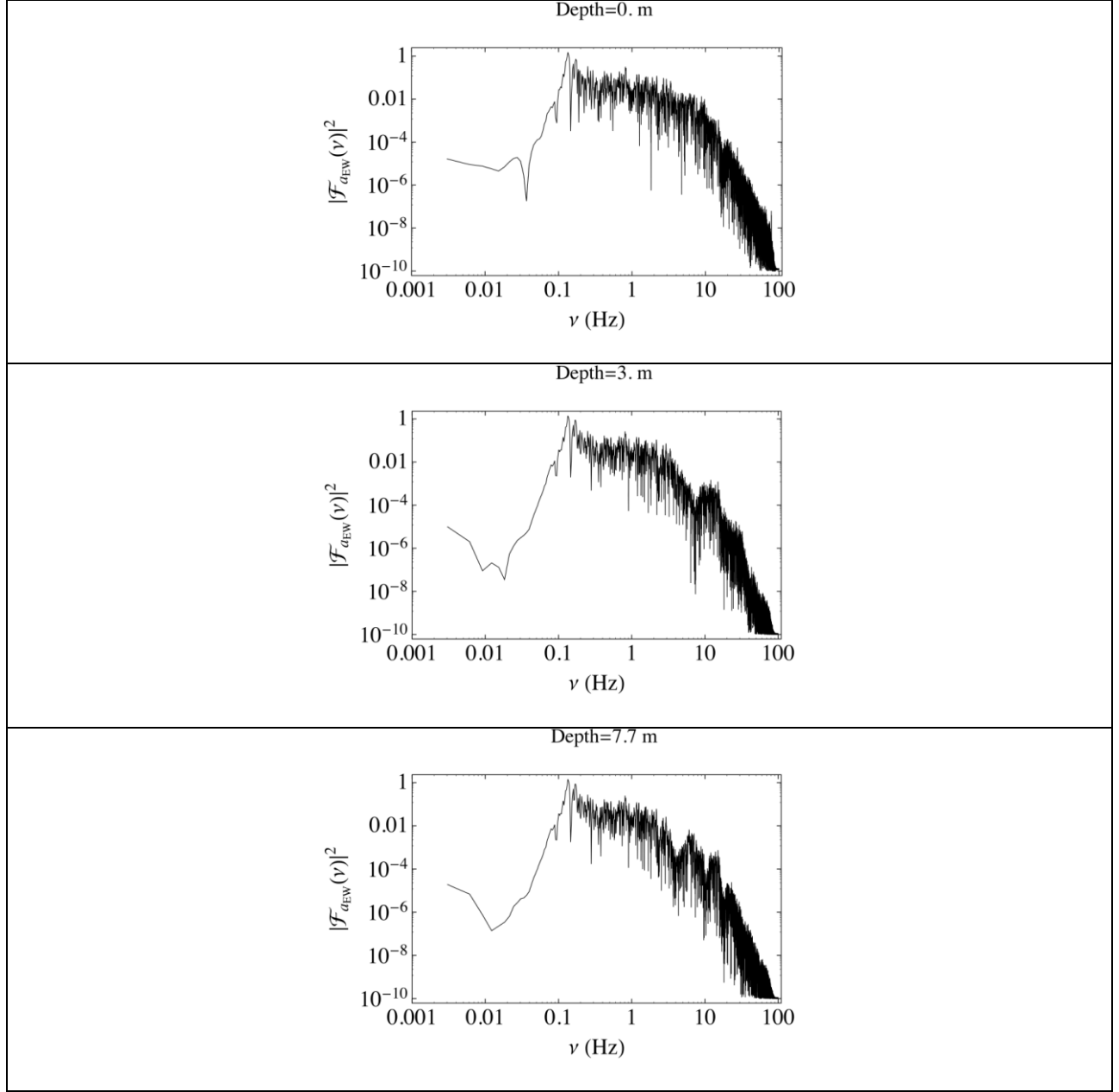


Figure 3.3: From top to bottom, the spectral curves $|\mathcal{F}_{a_{EW}}(\nu)|^2$ of the EW component of the acceleration a_{EW} reported in Figure 2.4.

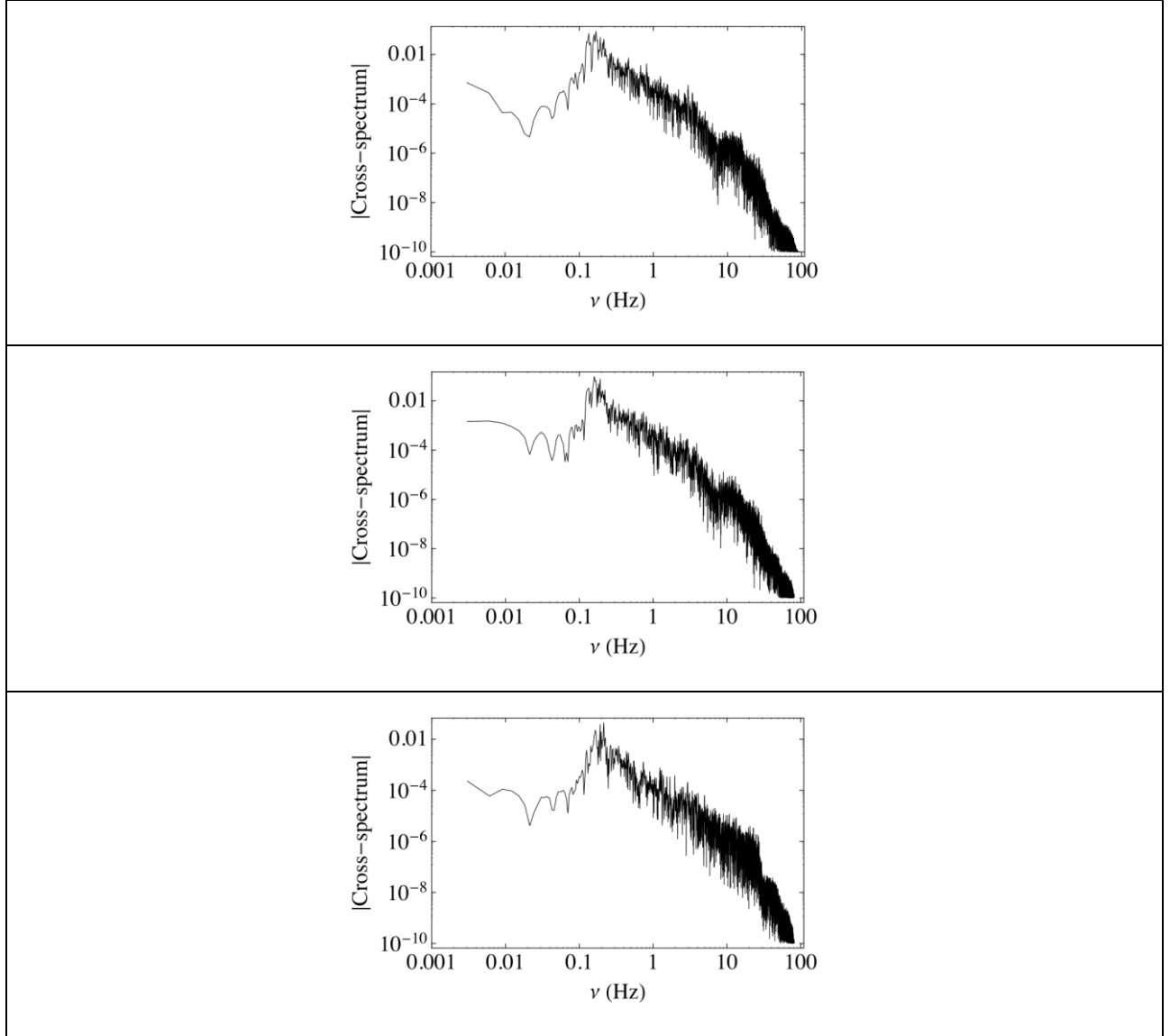


Figure 3.4: The top plot represents the amplitude of the cross-spectrum of the pore pressure time series observed at 3.4 m with the EW component of the acceleration recorded at 3 m. The cross-spectrum combine some of the features reported for $|F_p(\nu)|^2$ (see top plot in Figure 3.2) and $|F_{a_{EW}}(\nu)|^2$ (see middle plot in Figure 3.3). This is more obvious at low frequencies. Also note the depletions of the spectral curves at several frequencies in the range of 1 to 20 Hz. The amplitude of the cross-spectrum of the pore pressure time series observed at 3.4 m with the NS component of the acceleration recorded at 3 m. is given on the second plot. The amplitude of the cross-spectrum of the pore pressure time series observed at 3.4 m with the vertical component of the acceleration recorded at 3 m. is illustrated in the bottom plot.

4. WAVELET FORMALISM

4.1 A brief introduction

The wavelet representation is the natural approach to investigate time histories with a frequency content that varies in time. Such is the case for the recorded pore pressure and ground motion recorded during the 2010 Sierra el Mayor-Cucapah at the USGS Wildlife station (see Figures 2.3 and 2.4).

A wavelet transform can be understood as the convolution of the signal with a mother wavelet function. The mother wavelet $\psi((t - b)/a)$ is characterized by two parameters. One parameter a controls the dilatation (or contraction) of the width of the mother wavelet while the second parameter b controls the translation and thus the position of the mother wavelet in the signal. The wavelet transform decomposes the signal at different resolutions (or frequencies) while preserving important time dependent features such as phase arrivals. Wavelet coefficients result from computing the wavelet transform of a given signal and representing the signal in the scale-time domain or frequency-time domain. High-scale coefficients capture the fine structure embedded in the signal while low-scale coefficients characterize its coarse features. Wavelet transform “offers the flexibility of a genuine mathematical microscope that can focus on details on the signal at arbitrary positions and scales” (Sornette, 2004, p. 146).

Wavelets can be divided into two classes: continuous and discrete. Baker (2007) discussed the advantages and disadvantages of using continuous versus discrete wavelet transformations. For the project discussed here, we decompose the seismic signals using orthogonal discrete wavelet transform. For an orthogonal basis, the signal information captured by one wavelet coefficient doesn't overlap the information captured by the other coefficients. Just as for the Fourier transform, the square norm of the signal is preserved, *i.e.*, the square norm of all the wavelet coefficients is equal to the square norm of the original signal. These two features are necessary to properly compare the two signals and to quantify the interdependence between these two signals in the time-frequency domain.

A large literature is available that goes beyond the brief overview of wavelet properties presented here: Chui (1992); Ogden (1997); and Mallat (1998). There is also a manuscript dedicated to discrete wavelet transforms (Jensen and la Cour-Harbo, 2001). A recent review of the applications of wavelets in seismology is given in D'Auria *et al.* (2010) and references therein.

4.2 The Haar basis

For each signal considered in this study, the orthogonal wavelet basis is given by the Haar wavelet (corresponding to a Daubechies wavelet of order 0). The Haar wavelet (or mother) function is given by this expression:

$$\psi(t) = \begin{cases} 1 & 0 \leq t < 1/2 \\ -1 & 1/2 \leq t < 1 \\ 0 & \text{otherwise} \end{cases} \quad (4.1)$$

and the Haar scaling (or father) function is given by this expression:

$$f(t) = \begin{cases} 1 & 0 \leq t < 1 \\ 0 & \text{otherwise} \end{cases} \quad (4.2)$$

Figure 4.1 shows a schematic illustration of the wavelet decomposition, the Haar wavelet and Haar scaling functions. When convolved to a function, the wavelet and scaling functions of the Haar basis can easily be interpreted as a moving difference operator and a moving averaging operator. These operators respectively correspond to high pass and low pass filters. The differencing characteristics of the Haar wavelet function make it a good choice to analyze intermittent signals such as the velocity components of turbulent flows (Katul *et al.*, 1994). Since the wavelet is of finite width, it has a compact support. According to Katul and Parlange (1995), this property is very useful in quantifying the rapid variations observed in turbulent signals. Note that although the Haar basis is compact in the time domain, it is not compact in the Fourier domain since it decays very slowly as η^{-1} .

Haar wavelets have been used to investigate turbulent flows in the time and frequency domains (or space and wavenumber domains), see Meneveau (1991), Katul *et al.* (1994); Katul and Parlange (1995); Kulkarni *et al.* (1999); Papanicolaou and Solna (2003). Additional applications of the Haar wavelet can be found in the literature (Unser, 1995; Lindsay *et al.*, 1996; Bruce *et al.*, 2002; and Misiti *et al.*, 2007). Closer to seismology, Tibuleac and Herrin (1999) and Tibuleac *et al.* (2003) used the Haar wavelet for phase identification.

4.3 From wavelet scale to the Fourier frequency

Wavelet coefficients are displayed in Figure 4.1. Two parameters are needed to specify the functional dependence of the wavelet coefficients $d_{i,j}(f)$ of the function f : the scale and the time position at a given scale. On a dyadic grid, the scale is given by 2^i and the time position at the i^{th} scale is given by $j \times 2^i \times \Delta t$, where i and j are positive integers and Δt is the sampling time of the signal. On a typical scalogram, a 2D graphic representation of the wavelet coefficients, the horizontal axis shows the position in time while the vertical axis accounts for the scale either using the scale itself 2^i or the scale level (or index) i . It is sometimes more convenient to describe the distribution of the wavelet coefficients as a function of time and frequency (or space and wavenumber). For instance, in many investigations, it is necessary to compare the Fourier spectrum at a given frequency to the wavelet spectrum at a given scale (for details see Meneveau, 1991; Katul *et al.*, 1994; Katul and Parlange, 1995; and Addison, 2002). The comparison requires the calibration of the wavelet scale spectrum with the Fourier frequency or wavenumber. The calibration involves a reference period, or time interval, or a frequency. It can also be represented by a scale length or wavenumber. A common (and perhaps the simplest) definition adopted for the reference frequency η_s is given by the following expression:

$$\nu_s = 1/\Delta t \quad (4.3)$$

where Δt is the sampling time. The Fourier frequency η_i associated with the wavelet scale 2^i is given by the following expression:

$$\nu_i = 1/2^i \Delta t = \nu_s / 2^i \quad (4.4)$$

The calibration given by Eq. (4.4) is often used in the literature, see Meneveau (1991), Katul *et al.* (1994); Katul and Parlange (1995); Lindsay *et al.* (1996); Wilkinson and Cox (1996); Smith *et al.* (1998); and Papanicolaou and Solna (2003). This is also the relationship adopted in this paper.

Another relation is discussed in Riera-Guasp *et al.* (2008). A frequency band is associated to a given scale level i by the following relation:

$$\left[2^{-(i+1)} n_s, 2^{-i} n_s \right] \quad i = 1, 2, \dots \quad (4.5)$$

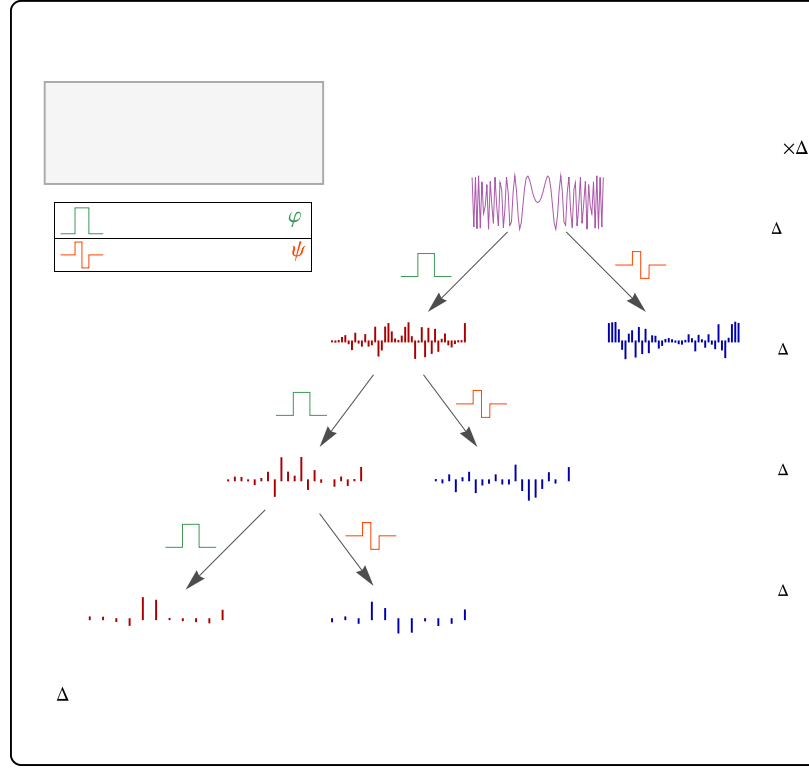


Figure 4.1: Schematic illustration of discrete wavelet decomposition. The original time t dependent signal (purple) with a resolution Δt is decomposed into two sets of coefficients, each with a resolution $2 \Delta t$. Convolution of the original signal with the wavelet function $y(t)$ gives the wavelet coefficients (blue). The wavelet coefficients are also denoted *details* or *detail coefficients*. The wavelet coefficient measures the amount of fluctuations in the signal about a given location t (Ogden, 1997). Convolution of the original signal with the scaling function $j(t)$ gives the coarser coefficients (red). The coarser coefficients are also called *approximations*, *approximation coefficients* or *scaling function coefficients*. The same operations are repeated to the coarser version of the signal (red) to get two new sets of wavelet coefficients at a lower resolution. The left side of the diagram schematically represents these operations. Note that at coarser resolutions the number of coefficients decreases. All the results discussed in this paper are based on the Haar wavelet transform. The scaling and wavelet functions for the Haar basis are illustrated in the schema.

The choice of a reference frequency is not unique. The choice can also be based on the properties of the Fourier spectrum of the mother wavelet $|F_\psi(\nu)|^2$. For instance, Addison (2002) suggests alternatives such as the spectral peak frequency or the pass band of the mother wavelet. The spectral peak frequency is the frequency for which $|F_\psi(\nu)|^2$ has a maximum, while the following relation defines the pass band of the mother wavelet:

$$\sqrt{\frac{\int_0^\infty \nu^2 |F_\psi(\nu)|^2 d\nu}{\int_0^\infty |F_\psi(\nu)|^2 d\nu}} \quad (4.6)$$

To relate the wavelet scale to the Fourier spectrum, Schneider and Farge (2001) define a mean wavenumber that is adapted to the time-frequency domain by defining the mean frequency associated to $|F_\psi(\nu)|$:

$$\frac{\int_0^\infty \nu |F_\psi(\nu)| d\nu}{\int_0^\infty |F_\psi(\nu)| d\nu} \quad (4.7)$$

Additional methods to derive a relationship between the wavelet scale and the Fourier frequency (or wavenumber) are discussed in Collineau and Brunet (1993) and Meyer *et al.* (1993).

According to Addison (2002), implementing an alternative reference frequency η_A is achieved by transforming Eq. (4.4) into $\nu_i = \nu_A / 2^i \Delta t = \nu_A \nu_S / 2^i$. This transformation is perhaps numerically correct but it is problematic since η_i is now proportional to the product of η_A by η_S !

For the Haar basis, the integral in the numerator of Eq. (4.6) and the integrals in the numerator and denominator of Eq. (4.7) don't converge. In the frequency domain, the spectral peak frequency for the Haar wavelet is equal to 0.74 and thus close to 1. Assuming that the contribution of the spectral peak frequency to the relation between frequency η_i and the wavelet scale 2^i (see Eq. 4.3) is given by a multiplicative factor, then ignoring this contribution (~ 1) will not significantly affect the results discussed in the following sections.

4.4 Computation of the wavelet transform and approximations

In this paper, the computation of the wavelet transform is based on the lifting wavelet transform implemented in Mathematica (version 8.0.1). First generation algorithms developed to compute discrete wavelet transform are based on convolution. The lifting wavelet transform is a second-generation algorithm using lifting steps to compute the transform (for additional details see Sweldens, 1997; Daubechies and Sweldens, 1998; and Jensen and la Cour-Harbo, 2001).

Finally, we address the issue of computing wavelet transforms of signals with finite duration. As pointed out in Jensen and la Cour-Harbo (2001; p. 2):

“But in the real world we always deal with finite length signals. There are problems at the beginning, and at the end, of a finite signal, when one wants to carry out a wavelet analysis of such a signal.”

To minimize distortions due to the finite length of the signal, we used Haar wavelets and considered signals with 2^N values, where $N = 16$. This is why the length of the seismic signals discussed in the third section is 327.675 seconds: $(2^N - 1)\Delta t = 327.675$ with $\Delta t = .005$ sec. To minimize distortions, we also used periodic padding at both ends of the seismic signal. The length of the seismic signals used in this work ensures that issues related to the finiteness of the signal will have a minimal impact on the results discussed in the next sections.

5. WAVELET TRANSFORM OF GROUND MOTION AND PORE PRESSURE TIME SERIES

Using lifting wavelet transforms with the Haar basis, we compute the wavelet coefficients of the ground motion and pore pressure recorded at the USGS Wildlife station during the 2010 Sierra el Mayor-Cucapah earthquake. Wavelet coefficients computed for the pore pressure time histories recorded at 3.4 m and the EW component of the ground motion recorded at 3.0 m are illustrated in Figures 5.1 and 5.2. For both signals, the time evolutions of the wavelet coefficients are illustrated for a range of frequencies that goes from 0.003 to 6.25 Hz. In both cases, the distributions of the wavelet coefficients are neither uniform nor a periodic function of time. One can identify time intervals where the wavelet coefficients have larger amplitudes compared to other time intervals. Both signals qualify as intermittent signals. The distributions of the wavelet coefficients as a function of frequency and time, illustrated in Figure 5.1, are representative of the distributions of the wavelet coefficients observed for pore pressure time histories recorded at 4.37 m and 5.74 m (see Figure 2.1). The same comment holds for the wavelet coefficients illustrated in figure 5.2 and those computed for other ground motions components recorded at identical or different depths.

At low frequencies (from 0.003 to 0.1 Hz) wavelet coefficients of the pore pressure illustrated in Figure 5.1 take large values in the first 150 seconds, with maximum values observed at 0.006 and 0.012 Hz. This suggests a significant contribution of low frequency oscillations to the pore pressure time series during the first 150 seconds. In the frequency range of 0.1 to 1 Hz, the wavelet coefficients contribute significantly to the signal even late in the signal. At higher frequencies, larger than 1 Hz, the wavelet coefficients take small values and there is almost no modulation of the wavelet amplitudes as a function of time.

The distribution of wavelet coefficients for the EW component of the ground motion in Figure 5.2 is quite different from the distribution of wavelet coefficients of the pore pressure time series. The most significant differences are observed at the low and high frequencies. At low frequencies (from 0.003 to 0.05 Hz), the wavelet coefficient values are very small when compared to the wavelet amplitudes at frequencies larger than 0.05 Hz. For frequencies larger than 0.05 Hz, wavelet coefficients contribute significantly to the signal, although the time dependency varies significantly from one frequency to another. For instance, large wavelet amplitudes are observed early in the signal for frequencies larger than 0.4 Hz, while the largest wavelet coefficients are observed later in time for coefficients with frequencies varying between 0.05 and 0.5 Hz. The largest wavelet amplitudes are observed at 0.781 and 0.195 Hz

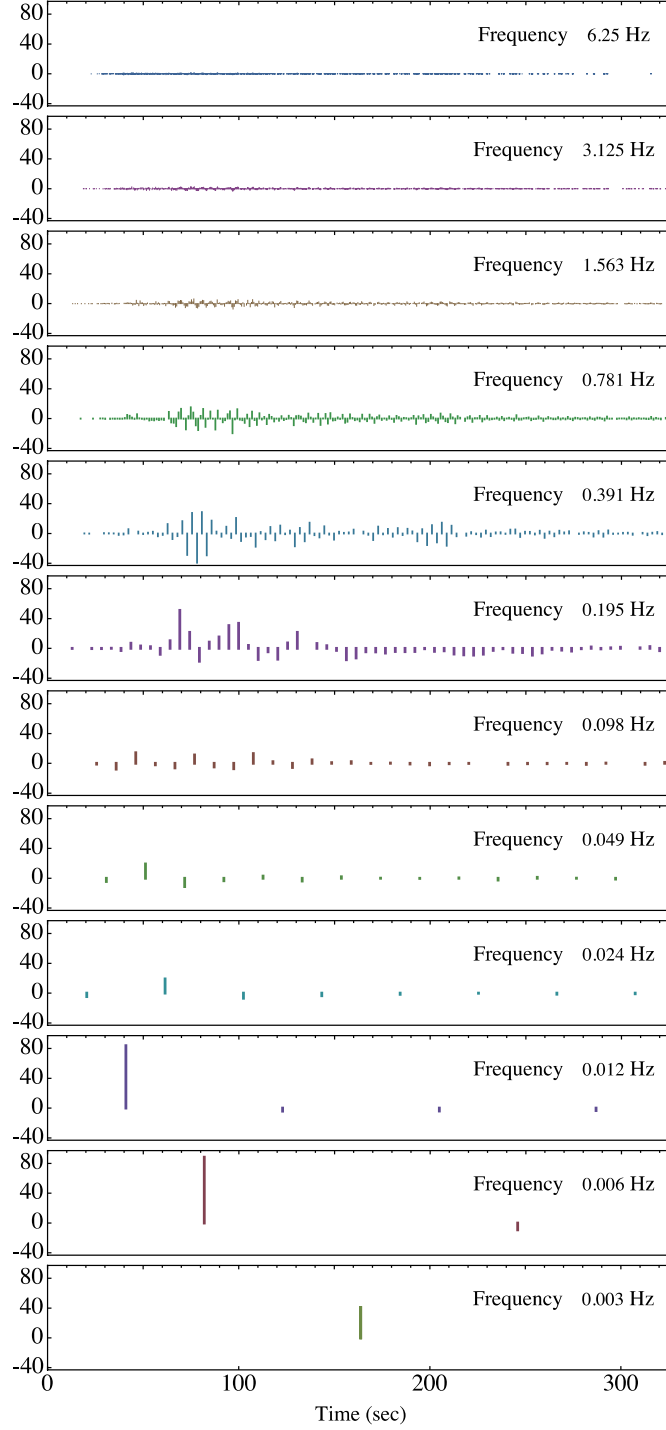


Figure 5.1: Examples of computed Haar wavelet coefficients for the pore pressure recorded at 3.4m - see also Figure 2.3. The distributions of wavelet coefficients illustrate the variability of the signals as a function of frequency as well as the strong time dependency. Note the large amplitudes of the wavelet coefficients of the pore pressure at low frequency and early in the signal. At the corresponding frequencies, the amplitudes of the wavelet coefficients associated to the ground motion are close to 0 (see Figure 5.2). Wavelet coefficients at high frequencies are not illustrated here.

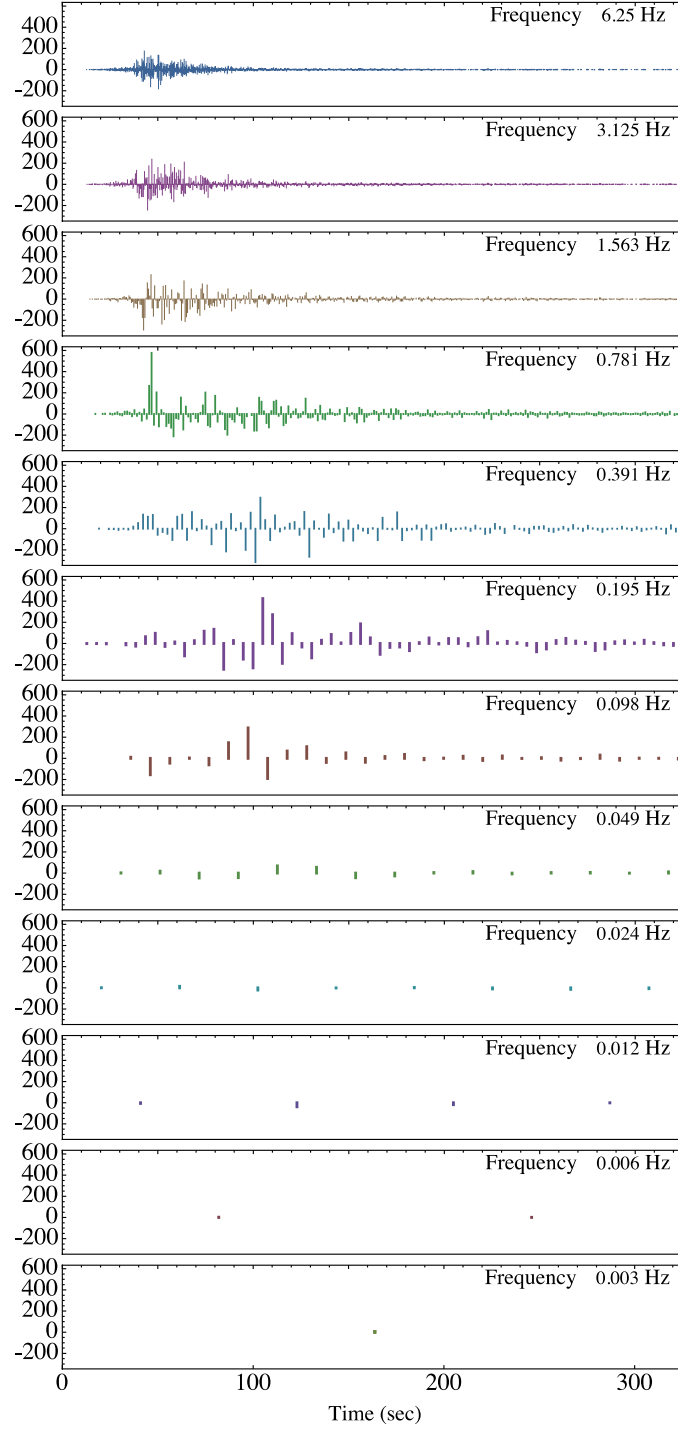


Figure 5.2: Examples of computed Haar wavelet coefficients for the EW component of the acceleration recorded at 3m - see also Figure 2.4. Wavelet coefficients at high frequencies are not illustrated here.

The distributions of the wavelet coefficients provide meaningful information about the pore pressure or ground motion time series. The interpretation of these distributions is unique to

each sample. It remains difficult to draw any conclusion about the interdependence of the two signals under observation (whether the two signals are both pore pressure time series, both ground time series, or ground motion and pore pressure time series). In the next section, we will discuss two tools that may help capture and quantify the coupling between two signals and the relevance of the coupling.

6. MULTIPLE SCALE ANALYSIS

6.1 The wavelet correlation and the square norm ratio

The proper framework to study the interdependence of two intermittent signals at different resolutions and/or frequencies is provided by wavelet analysis. Given this framework, we propose to combine two concepts to characterize the features shared by a pair of signals while taking into account the localization of the feature as well as the relative contribution of these features to their respective signals.

The first concept is the *wavelet correlation*, which identifies common features in the two signals and quantifies a potential linear –or quasi-linear- dependency between the two signals. It is given by computing the correlation of the wavelet coefficients as a function of the scale or the frequency (Percival and Walden, 2000). The wavelet correlation $\mathcal{W}r_i(f, g)$ at scale 2^i is defined by the following relationship

$$\mathcal{W}r_i(f, g) = \frac{\sum_{j=1}^{2^i} (d_{i,j}(f) - \overline{d_i(f)}) (d_{i,j}(g) - \overline{d_i(g)})}{\sqrt{\sum_{j=1}^{2^i} (d_{i,j}(f) - \overline{d_i(f)})^2} \sqrt{\sum_{j=1}^{2^i} (d_{i,j}(g) - \overline{d_i(g)})^2}} \quad (6.1)$$

where $d_{i,j}(f)$ and $d_{i,j}(g)$ are respectively the wavelet coefficients of the functions (or signals) f and g . The variables $\overline{d_i(f)}$ and $\overline{d_i(g)}$ are respectively the means of the wavelet coefficients $d_{i,j}(f)$ and $d_{i,j}(g)$ at scale 2^i . The wavelet correlation defined in Eq. (6.1) takes values between -1 and 1.

Note that the wavelet correlation is not a generalization of the lagged cross-correlation (or its counterpart in the frequency domain the cross-spectrum discussed in Section 3). The lagged cross-correlation between the two signals f and g with lag t is given by $\int g(t)f(t+t)dt$ and quantifies the likelihood to find common features between f and g separated by an interval t . The wavelet correlation quantifies the likelihood to find common features between f and g as a function of scale, but around the same time interval! The concept of lagged (or delayed) wavelet correlation is closer to the concept of lagged cross-correlation.

Wilkinson and Cox (1996) compute the lagged wavelet correlation for the wavelet coefficients of two signals at two specific scales. In their paper, the authors use Daubechies wavelets to compare two signals generated by turbine vibrations. A similar concept of lagged wavelet cross-correlation is also discussed in van Milligen (1999) for continuous wavelets with application to plasma. In Eq. (6.1), the lag is set to 0. The expression in Eq. (6.1) can also be seen as a generalization of the concept of *scale correlation*, as defined for a single signal in Addison *et*

al. (2001). Using the wavelet framework, and based on the concept of correlations, different tools have been discussed in the literature to compare two signals (e.g.: Liu, 1994; Torrence and Compo, 1998; van Milligen, 1999; Addison, 2002; Papanicolaou and Solna, 2003; Misiti *et al.*, 2007; and Adamowski, 2008).

The wavelet correlation provides a quantitative measure that describes the common features shared by two signals at a given scale 2^i . To complement this measure, it is also necessary to quantify the contribution of these features to their respective signals. For this purpose, a second concept is used. The *square norm ratio* quantifies the relative strength or weight of wavelet coefficients at a given scale to the total strength of the signal. It identifies the contribution of the most dominant wavelet coefficients necessary to reconstruct the signal. The square norm ratio $\mathcal{N}_i^2(f)$ of the function (or signal) f at scale 2^i is given by the following relationship:

$$\mathcal{N}_i^2(f) = \frac{\sum_{j=1}^{2^i} |d_{i,j}(f)|^2}{\sum_{i=1}^{N_s} \sum_{j=1}^{2^i} |d_{i,j}(f)|^2} \quad (6.2)$$

where N_s is the number of scales used in the wavelet decomposition. (For a signal with 2^N values $N_s = N$.) Note that the denominator in Eq. (6.2) is equal to the square norm of the signal $|f|^2$, since the wavelet decomposition is computed with an orthogonal wavelet basis.

By combining the information given by the wavelet correlation and the square norm ratio, one can identify the strength of properties shared by a pair of signals. Note also that although both concepts, the wavelet correlation and the square norm ratio, are defined as a function of the scale, they can easily be given as a function of the frequency by using Eq. (4.4).

6.2 Evaluation of the wavelet correlation performance

According to the definition of the wavelet correlation in Eq. (6.1), the number of events in the sum is a function of the scale 2^i . The number of values at a given scale decreases rapidly as the scale level i increases or as the frequency n_i decreases (see Eq. 4.4). When estimating the robustness of a statistical parameter, the larger the number of values used in computing the parameter, the more accurate is the estimate. It is assumed that convergence to the “*real*” estimate of a statistical parameter is achieved when the number of values to compute the statistical parameter is large enough. Thus, to assess the performance and robustness of the wavelet correlation values computed at a given scale (or frequency), the following numerical experiment is designed.

1. Generate 500 independent stochastic time series with a number of events identical to the number of events in the acceleration or pore pressure time series. The stochastic time series consists of a Gaussian white noise with mean equal to 0 and standard deviation equal to 1.
2. For each stochastic time series, compute the wavelet correlation between the stochastic time series and the EW component of the acceleration recorded at 0 m.
3. At each given frequency, compute the mean for the 500 wavelet correlation values.

4. At each given frequency, compute the standard deviation for the 500 wavelet correlation values.

The results of the computation discussed above are illustrated in Figure 6.1. The mean wavelet correlations are close to 0 at every frequency, and thus frequency independent. The standard deviation for the multiple scale correlation, represented by the brown area in Figure 7, decreases with the frequency value. Similar results are obtained when performing the same numerical experiments with other seismic signals in place of the EW component of the accelerations. The result is illustrated for the pore pressure time series in Figure 6.2. The same results are also obtained when repeating the same computation for 1000 independent stochastic time series.

Based on these results, we propose the adoption of the following rule to assess the robustness or reliability of the wavelet correlation values for two signals computed at a given frequency. For two signals, a wavelet correlation value that is within one standard deviation value of the wavelet correlation value estimated in this section performs as well “in average” as a wavelet correlation for a Gaussian white noise and one of the two signals. That is, the cross-correlation value cannot be discriminated “in average” from the cross-correlation between a Gaussian white noise and one of the two signals. A wavelet correlation value that is outside one standard deviation value of the wavelet correlation value estimated in this section is considered a significant and meaningful estimate of the cross-correlation. The standard deviation reported in Figure 6.1 is used as a reference for all the seismic signals discussed in the next section.

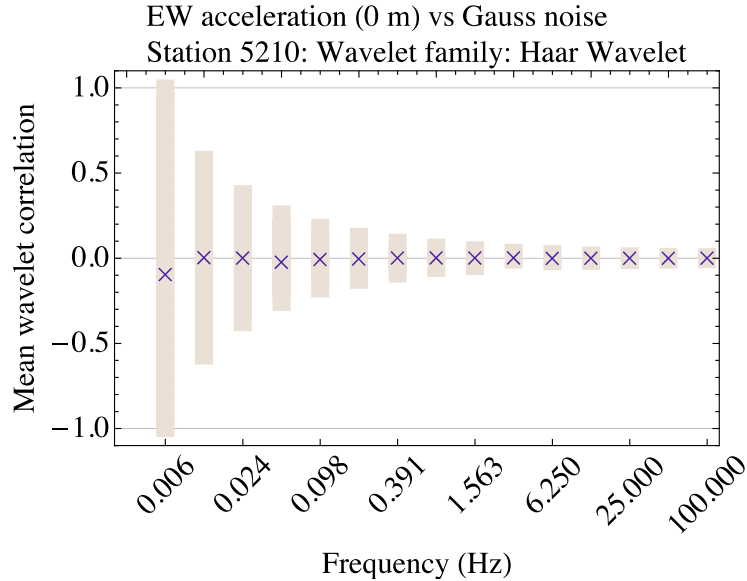


Figure 6.1: Computation of the mean for the 500 multiple scale correlation values between a stochastic time series and the EW component of the acceleration. The mean correlation is near 0 at every frequency. At every scale, the brown area corresponds to the range of values located between plus-or-minus the standard deviation for the 500 multiple scale correlation values between a stochastic time series and the EW component of the acceleration. The vertical size of the brown area decreases with the frequency. Statistically, it is much more difficult to estimate the degree of linearity between two signals at low frequency.

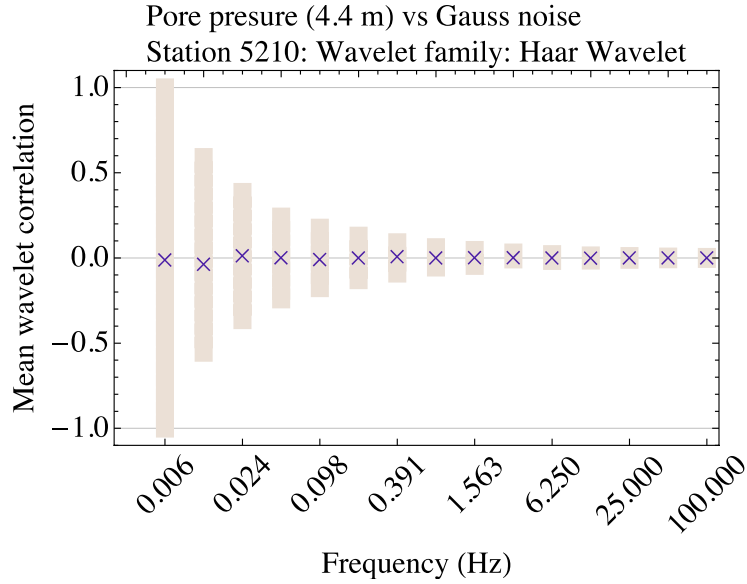


Figure 6.2: Same as Figure 6.1 but for the pore pressure time history.

7. WAVELET CORRELATION AND SQUARE NORM RATIO OF SEISMIC SIGNALS.

In this section, we discuss the computation of the wavelet correlation and the square norm ratio of the ground motion and pore pressure recorded at the USGS Wildlife station during the 2010 Sierra el Mayor-Cucapah earthquake. The computations are performed for different sets of seismic signals.

In addition to the recorded acceleration and pore pressure, we also include the ground motion velocity and the displacement in our analysis. Velocities and displacements are computed with numerical integration of the acceleration records. The acceleration records are filtered in Matlab with a Butterworth filter that has a pass band from 20 sec to 50 Hz. The mean is removed from the signal before each integration is performed.

7.1 Ground motion time series

The first set includes the EW components of the acceleration recorded at different depths, see Figure 2.4. The correlations between the wavelet coefficients of the EW components of the acceleration recorded at different depths are shown in Figure 7.1A. The corresponding square norm ratios are in Figure 7.1B. The curves in Figure 7.1A show that the wavelet coefficients are highly correlated for frequencies less than or equal to 3.125 Hz, with a small departure from this behavior observed at 0.024 Hz. For frequencies larger than 3.125 Hz, the correlation decreases quickly to zero as the frequency increases.

The sudden change in the wavelet correlations reported in Figure 7.1A can be understood in terms of wave propagation. As the seismic waves travel across the layered medium, oscillations shift in the time domain. Assuming plane waves propagating in the vertical direction, the amount of time shift between plane waves recorded at two instruments located at different depths can be estimated by computing the ratio between the distance separating the two instruments and the average shear-velocity in the layered medium. The frequency corresponding

to the amount of shift is thus given by the ratio between the average shear-velocity in the layered medium and the distance separating the two instruments.

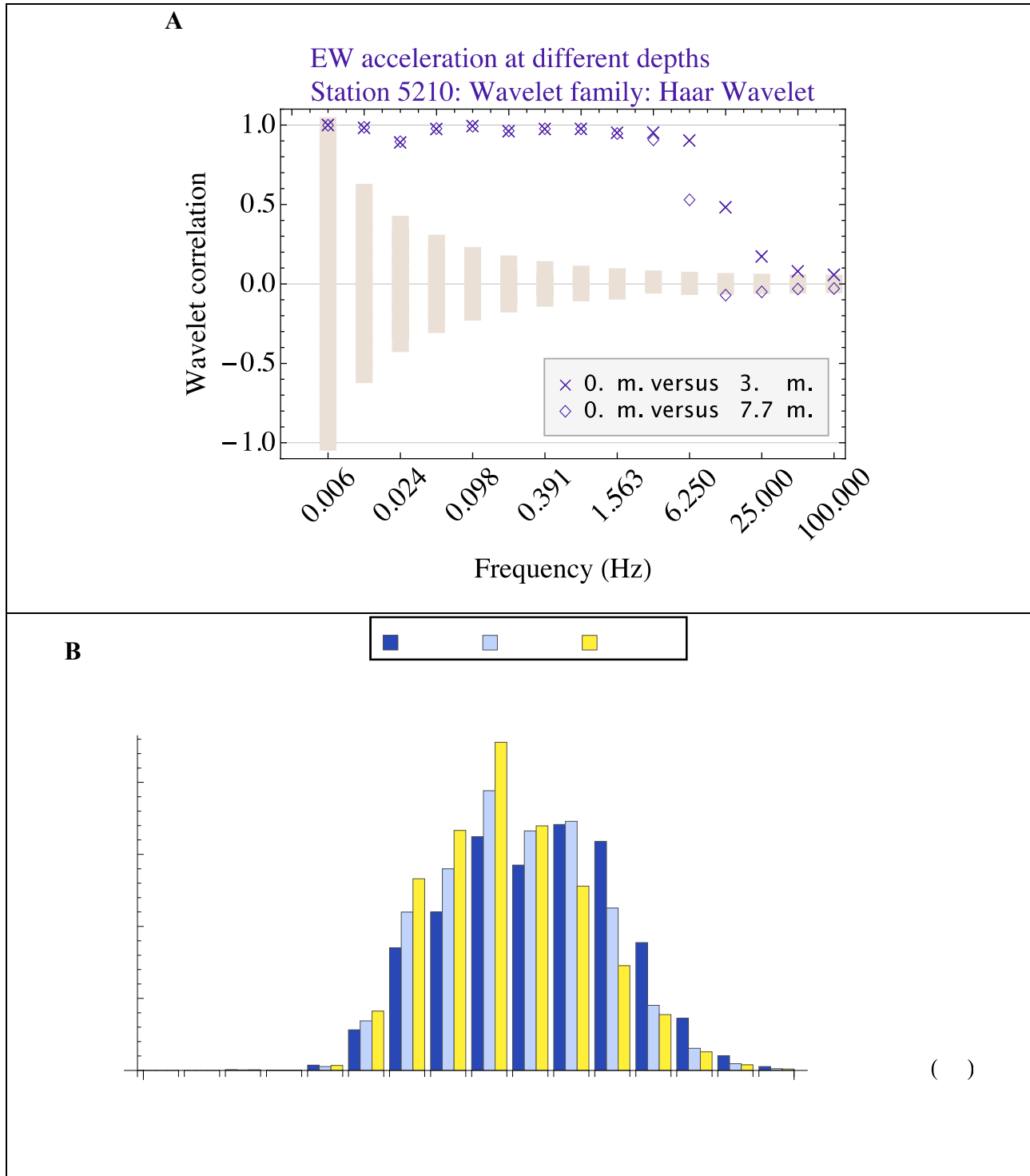


Figure 7.1: A. Computation of the wavelet correlation between the wavelet coefficients of the EW components of the acceleration recorded at different depths -see Figure 2.3. Except for high frequencies, the wavelet coefficients are well correlated and thus largely

independent of the depth. Note that the correlation between the component recorded at a depth of 0 m and the component recorded at a depth of 7.7 m (diamond shape symbols) asymptotes more quickly to 0 than the correlation between the component recorded at a depth of 0 m and the component recorded at a depth of 3 m (cross symbols). The meaning of the brown areas in the left plot is discussed in Section 6. **B.** Computation of the square norm ratio for the three EW components of the acceleration recorded at different depths. The distribution of the square norm ratio is largely independent of the depth at which the ground motion was recorded.

For the USGS Wildlife station (see Figure 1), SCPT logs indicate that the shear wave velocity varies from 100 m/sec at the surface to a maximum value of 170 m/sec at 7.5 m depth, with average values on the order of 130 m/sec (data from site testing are available at <http://www.nees.ucsb.edu/facilities/wla>). The frequencies corresponding to these values for station separated by a 7.7 m distance are respectively 13 Hz, 22.1 Hz and 16.9 Hz. In Figure 7.1A, the correlation between wavelet coefficients at 0 m and at 7.7 m reach a value close to 0 at 12.5 m and remains close to 0 for higher frequency values.

Wavelet coefficients at a given scale and location are computed for a finite time interval or time window. The time window at a given scale is $2^i \Delta t$ with a Fourier frequency η_i (see Eq. 4.4). The duration of the time window is the distance between two consecutive vertical bars in Figures 5.1 and 5.2. For a given location and for a large time window, the wavelet coefficients estimated at 0 m and 7.7 m are almost the same since the average time shift ($\sim 1/16.9 \text{ Hz} \sim 0.6 \text{ sec}$) of the wave as it travels over a distance of 7.7 m is very small compared to the duration of the time window. The situation is different for small time windows (or high frequencies) with durations similar to or smaller than the amount of shift due to the wave travelling between the two stations. For a given location, the estimated wavelet coefficients at 7.7 m are based on oscillations that are largely or completely shifted to another time window when these oscillations are recorded at 0 m. Thus, for a given location and for a small time window, the wavelet coefficients estimated at 0 m and 7.7 m are based on oscillations that are significantly or completely different from the others. For these small windows (high frequencies), the wavelet coefficients at 0 m and 7.7 m are poorly correlated, which is the situation depicted by the curves in Figure 7.1A. Note that, as expected, the correlation curve for the wavelet coefficients corresponding to the acceleration recorded at a larger distance (0 m versus 7.7 m) decreased more rapidly when compared to the correlation for the wavelet coefficients corresponding to the acceleration recorded at a closer distance (0 m versus 3 m).

The distributions of the square norm ratios are described by well-localized functions similar in shape. The curve corresponding to the acceleration recorded at 0 m has a single maximum and can be represented by a unimodal function. For frequencies less than or equal to 1.563 Hz, the square norm ratios are systematically attenuated as the depth of the observation decreases. For frequencies larger than or equal to 6.25 Hz, the square norm ratios amplified as the depth decreases.

The correlations between the wavelet coefficients of the NS components of the acceleration recorded at different depths are shown in Figure 7.2A. The corresponding square norm ratios are in Figure 7.2B. The functional behavior of the curves in Figure 7.2A is similar to Figure 7.2B. The distributions of the square norm ratios are also described by well-localized functions, although with a more complicated functional behavior than the distributions reported for the EW components in Figure 7.1A. Attenuation of the square norm ratios at low frequencies

as the depth decreases and amplification at higher frequencies as the depth increases is also observed in Figure 7.2B.

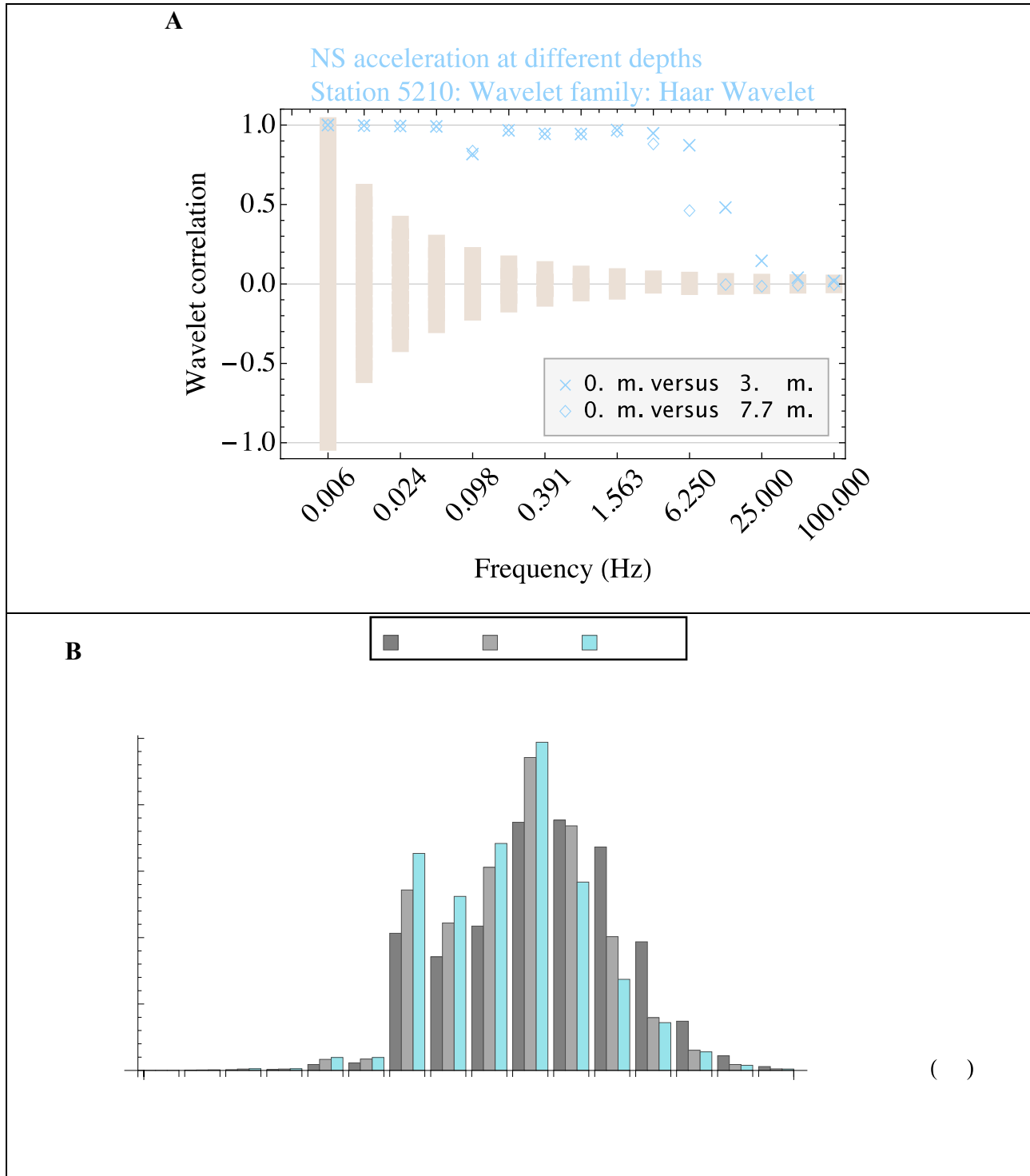


Figure 7.2: Same as Figure 7.1 but for the NS components of the acceleration.

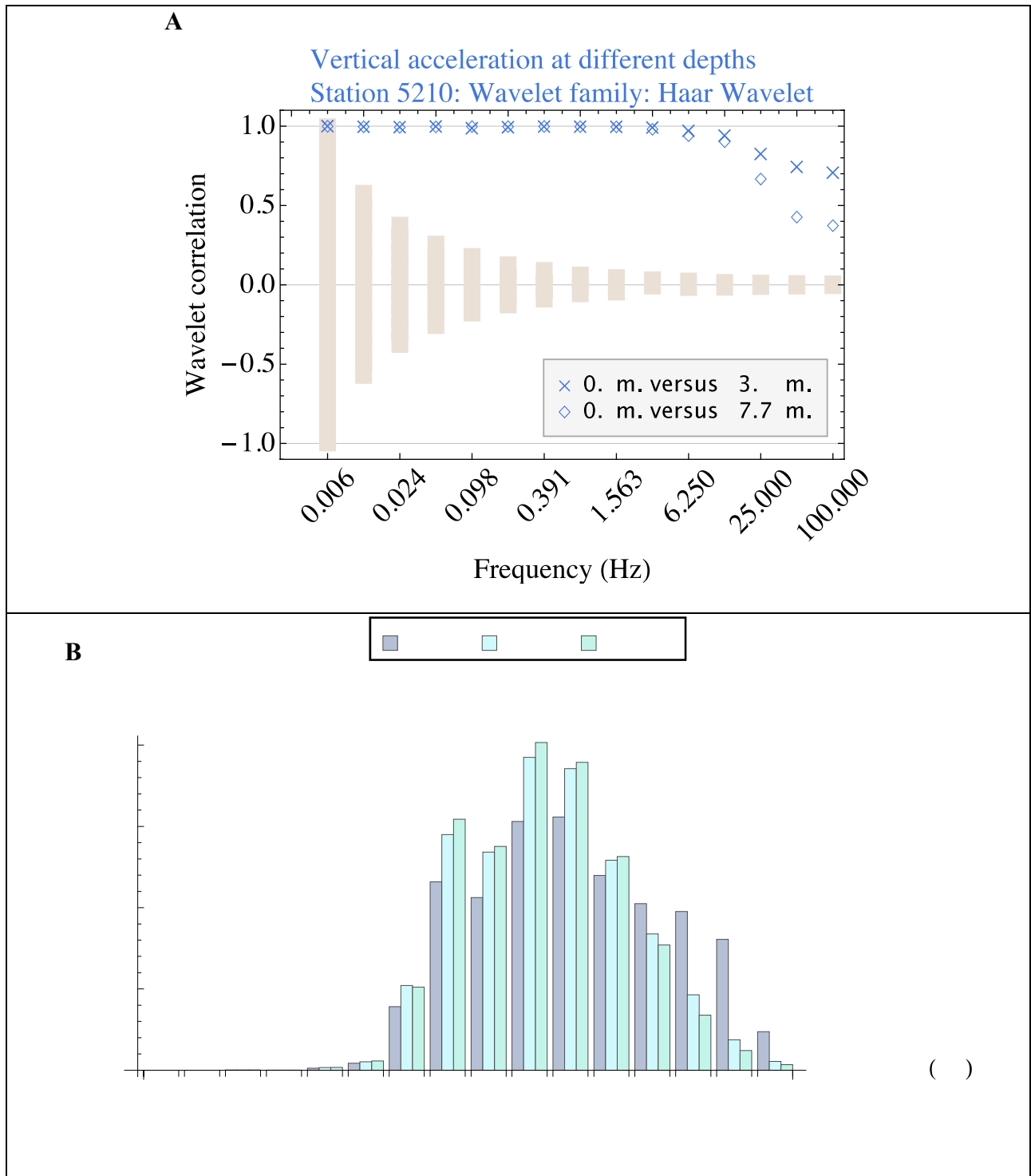


Figure 7.3: Same as Figure 7.1 but for the vertical components of the acceleration.

The correlations between the wavelet coefficients of the vertical components of the acceleration recorded at different depths are reported in Figure 7.3A. The corresponding square norm ratios are in Figure 7.3B. In Figure 7.3A, the correlation curves decrease at a slower pace at higher frequencies than the sharp attenuation reported in Figures 7.1A and 7.2A. Vertical

components are travelling with a P -wave velocity that is higher than shear wave velocity and will thus have a greater impact on the correlation curves at higher frequencies. For the vertical components, the distributions of the square norm ratios extend over a larger range of frequencies than the range reported in Figures 7.1B and 7.2B. Attenuation of the square norm ratios at low frequencies as the depth decreases and amplification at higher frequencies as the depth increases is also observed in Figure 7.3B.

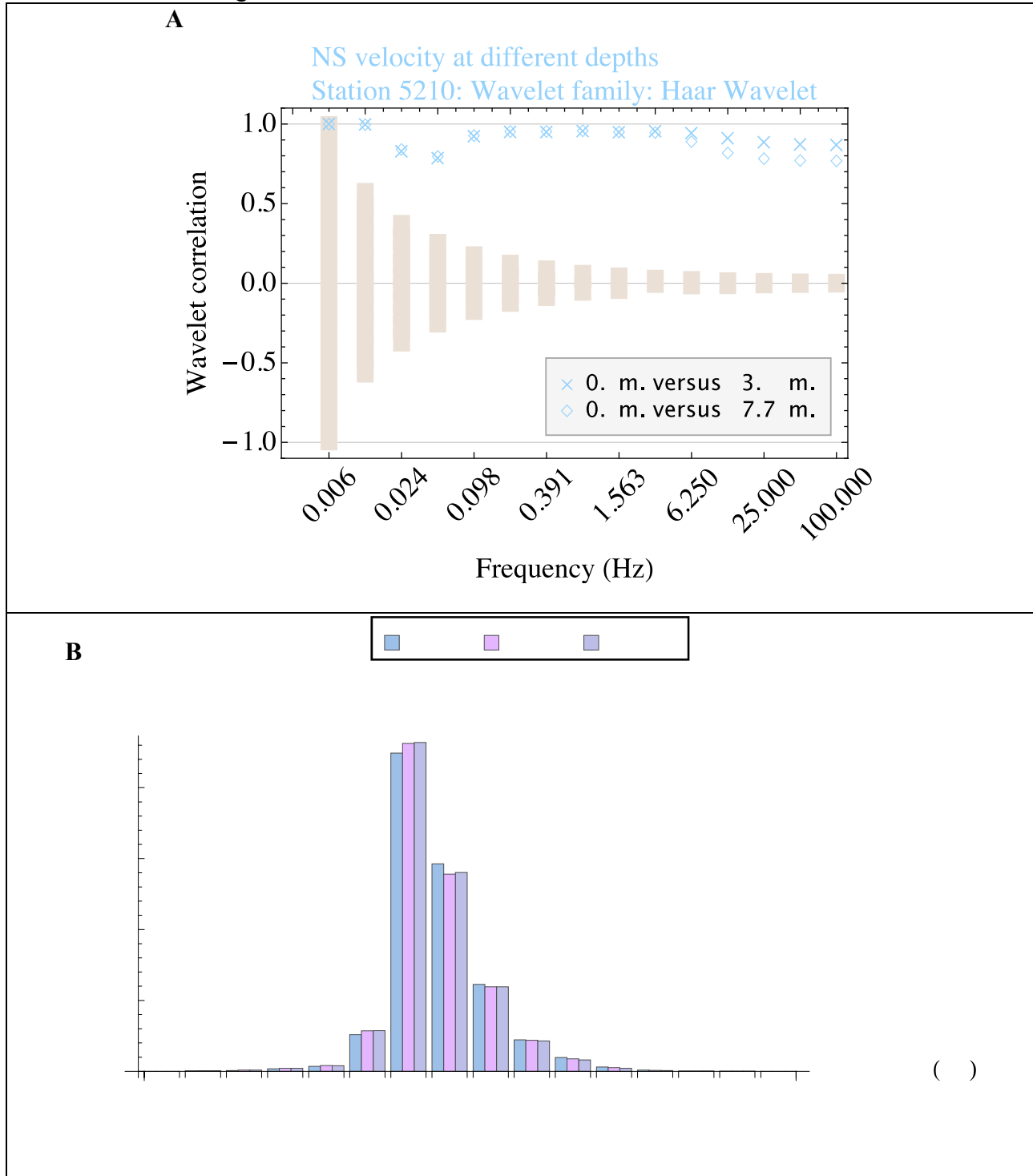


Figure 7.4: Same as Figure 7.1 but for the NS components of the velocity.

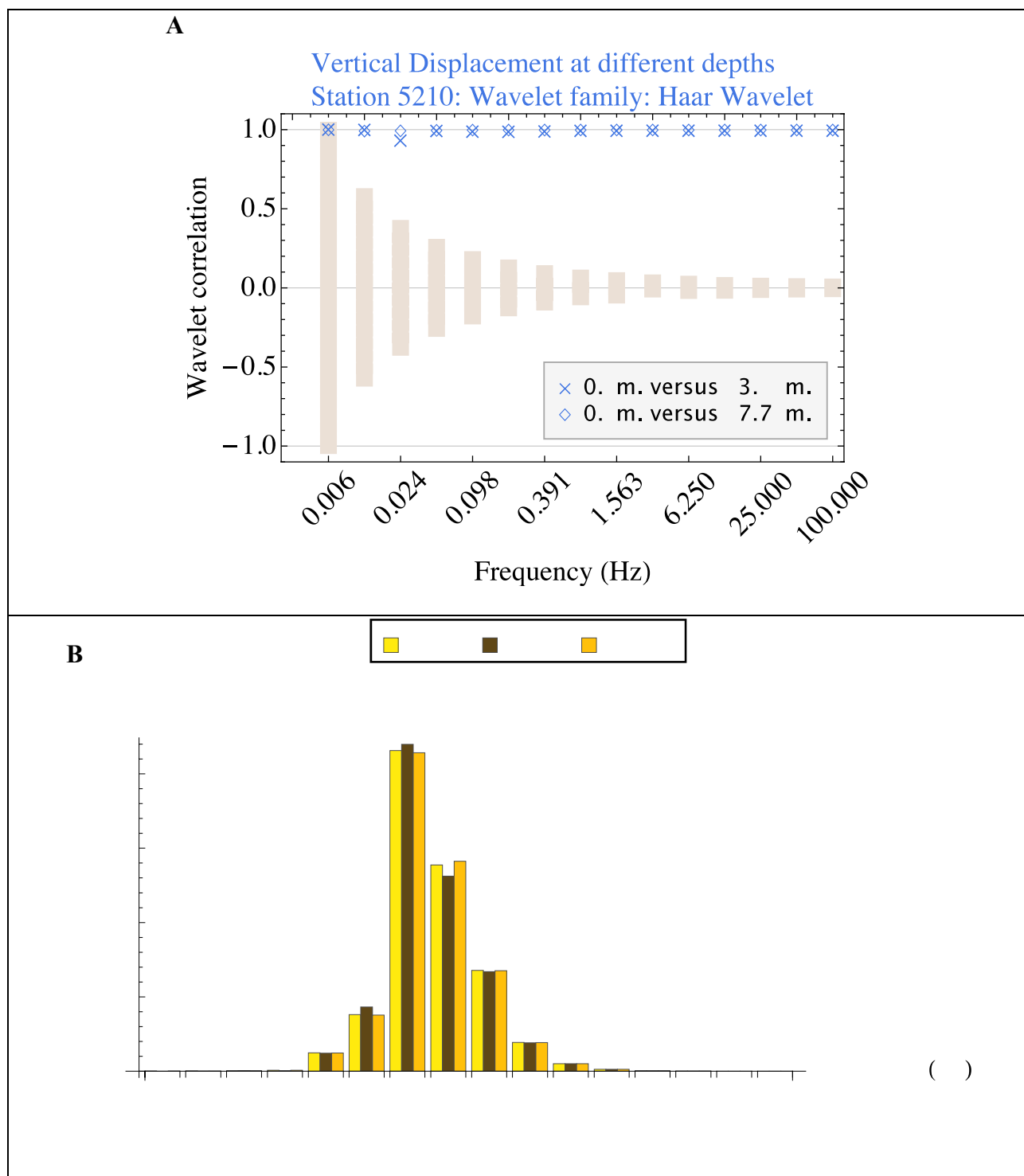


Figure 7.5: Same as Figure 7.1 but for the vertical components of the displacement.

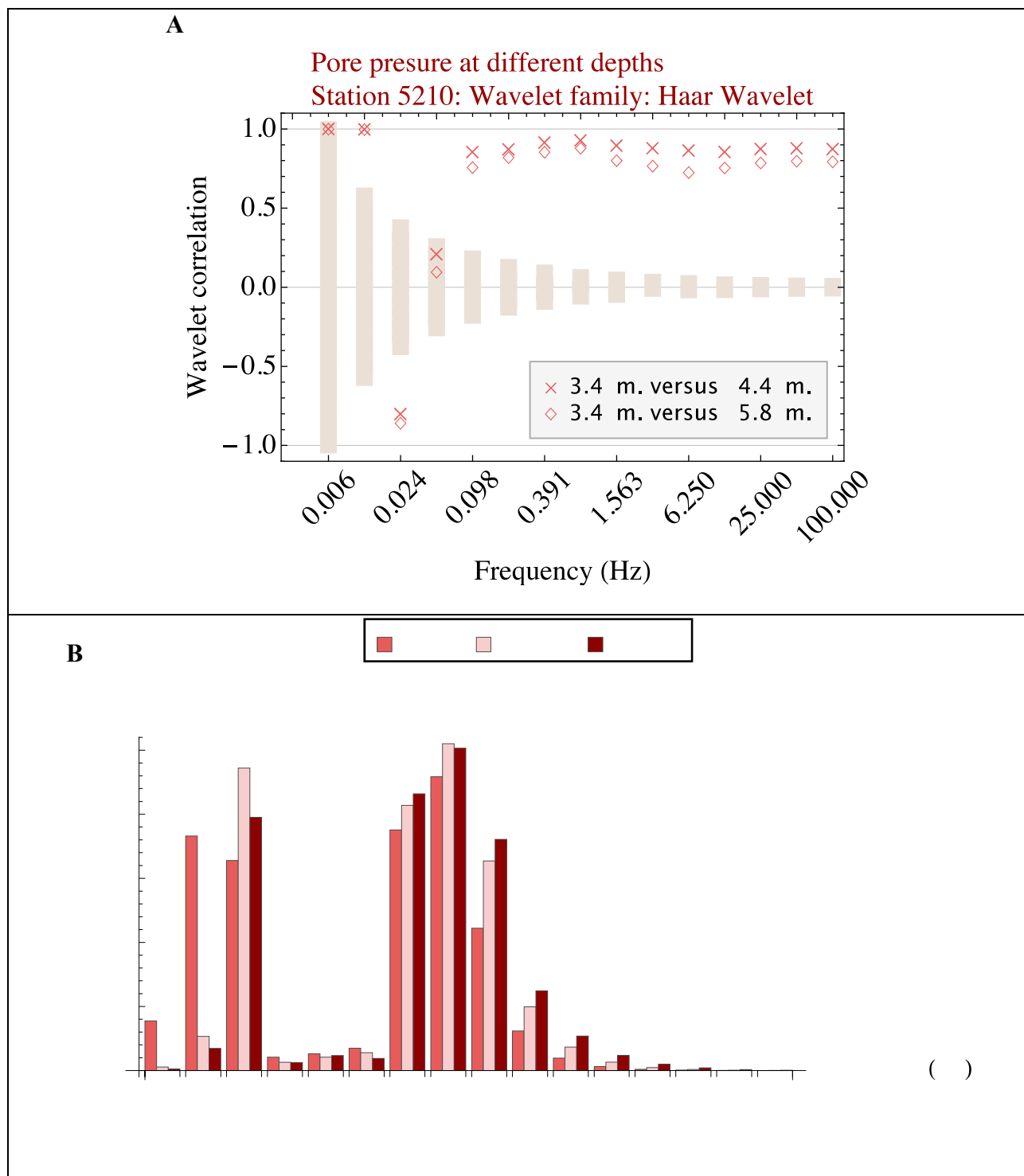


Figure 7.6: Same as Figure 7.1 but for the pore pressure.

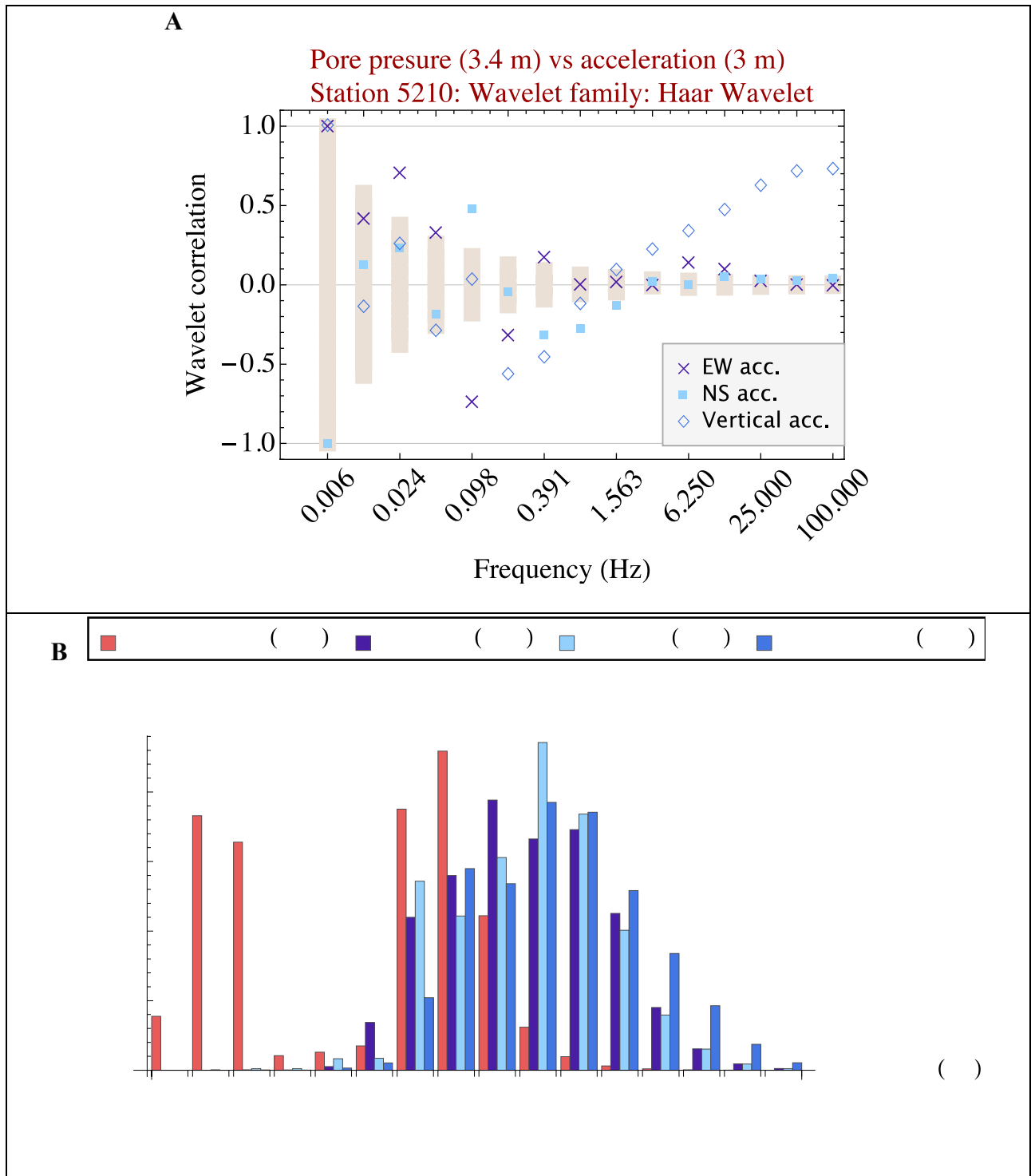


Figure 7.7: **A.** Computation of the wavelet correlation between the wavelet coefficients of the pore pressure and the wavelet coefficients of each component of the acceleration recorded at a similar depth (~3 m). **B.** The distribution of the wavelet coefficient of the acceleration are shifted to the high frequencies when compared to the distribution of the wavelet coefficient of pore pressure. Note the significant values of the square norm ratio

of the pore pressure at low frequencies with no correspondence for the square norm ratio of the acceleration components.

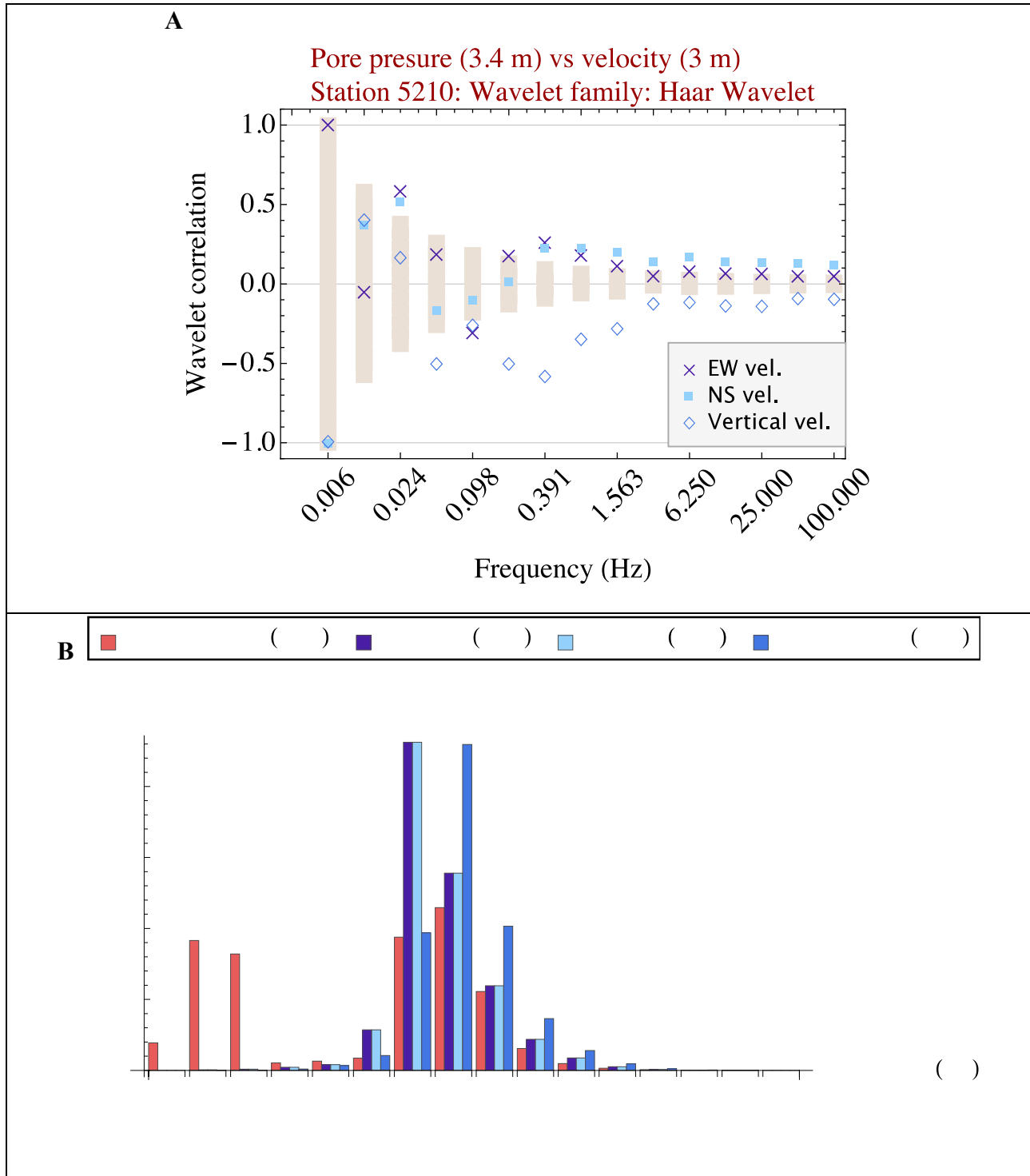


Figure 7.8: Same as Figure 7.7 but for the velocity components at a similar depth (~3 m).

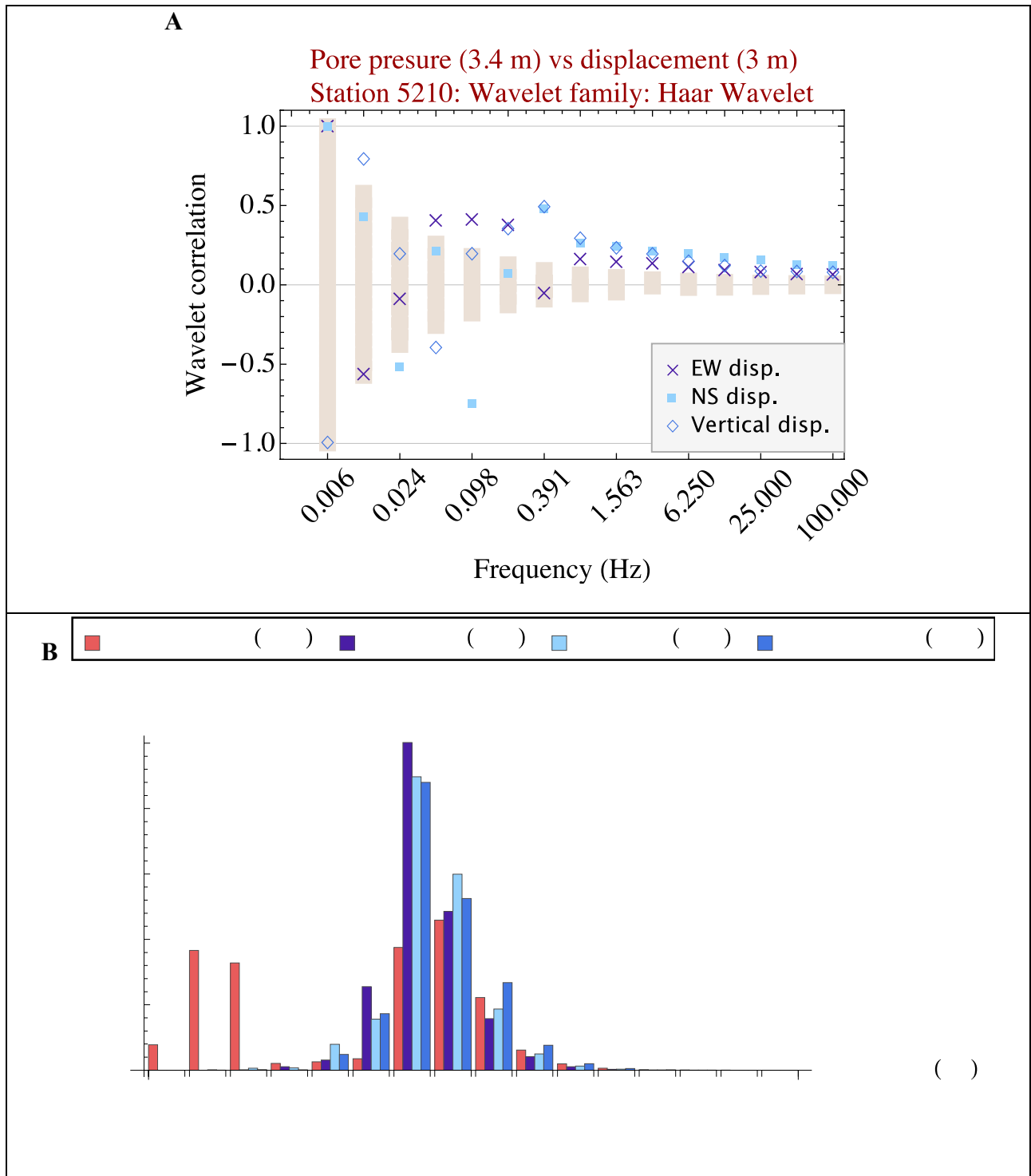


Figure 7.9: Same as Figure 7.7 but for the displacement components at a similar depth (~3 m).

Computations of the wavelet correlations and the square norm ratios for the three velocity components are rather similar. The same conclusion holds for the three displacement components. For this reason, we will only report the results for the NS component of the velocity

in Figure 7.4 and the results for the vertical components in Figure 7.5. The curves in Figure 7.4A show that the wavelet coefficients are highly correlated for all the frequency ranges. This result is not surprising since computation of the velocity and the displacement removes the high frequency components from the signal. The distributions of the square norm ratios illustrated in Figure 7.4B are quasi identical, and thus largely independent of the depth of the recording. These distributions are well described by a unimodal function with a maximum at 0.195 Hz. The same conclusions hold for the results illustrated in Figure 7.5. The results in Figure 7.4 and 7.5, which are similar to the other components of the velocity and of the displacement, suggest that, with the exception of small fluctuations, the velocity time histories and the displacement time histories are almost independent of the depth of the recording.

7.2 Pore pressure time series

In this sub-section, we consider the pore pressure time histories recorded at different depths, see Figure 2.3. The correlations between the wavelet coefficients of the pore pressure recorded at different depths are shown in Figure 7.6A. The corresponding square norm ratios are in Figure 7.6B. Except for the correlation at 0.024 Hz and 0.049 Hz, the wavelet coefficients are well correlated, with values close to 1. The values of the square norm ratios at 0.024 Hz and 0.049 Hz are very small, so departure from the behavior observed at other frequencies in Figure 7.6A can be ignored. The distributions of square norm ratios are characterized by large values at mid-range frequencies (frequencies between 0.195 Hz and 1.563 Hz) and at low frequencies (frequencies between 0.003 Hz and 0.012 Hz). In the mid-range frequencies, the shape of the distributions are similar from one depth to another. The shape corresponds to a unimodal function with a large jump at 0.195 Hz, a maximum observed at 0.395 Hz, and an attenuation at higher frequencies. At low frequencies, the distributions of square norm ratios strongly depend on the depths at which the pore pressure is recorded. Note that the large wavelet coefficients characterize are localized in the first half of the pore pressure time history (see Figure 5.1).

The distributions of the square norm ratio values for the pore pressure (figure 7.6) are quite different from those reported in Figures 7.1 to 7.5 for ground motions. The question is to determine the likelihood of a causal mechanism that relates the seismic waves and the variations observed in the pore pressure time histories that can be inferred from the wavelet decomposition.

7.3 Mixed seismic signals recorded at 3 m.

In this sub-section, we consider three data sets that include the pore pressure time histories recorded at 3.4 m and the three components of the ground motions recorded at 3 m, see Figures 2.3 and 2.4. We select data recorded at similar depths (~3 m) to minimize the depth dependence discussed in the two previous sub-sections.

The correlations between the wavelet coefficients of the pore pressure and the three components of the acceleration are shown in Figure 7.7A. The corresponding square norm ratios are in Figure 7.7B. The functional behavior of the correlation curves reported in Figure 7.7A is more complicated than the behaviors reported in Figures 7.1A to 7.6A. At high frequencies (frequencies between 3.125 Hz and 100 Hz), the correlations between the wavelet coefficients of the pore pressure and the wavelet coefficients of the vertical component of the acceleration increase with the frequency. At the corresponding frequencies, Figure 7.7B shows that the square norm ratio for the pore pressure is close to zero. At frequencies ranging from 0.012 Hz to 0.098 Hz, the EW components exhibit (in absolute value) the largest correlation with the pore pressure

wavelet coefficients. Also at the corresponding frequencies, Figure 7.7B shows that the square norm ratio for the three acceleration components is almost zero. Again, under the assumption of a linear or quasi-linear dependency between the pore pressure and the components of the acceleration, the large fluctuation observed in the distribution of the square norm ratio of the pore pressure at low frequencies (smaller than 0.024 Hz) can only result from a mechanism that will largely amplify the very small oscillations present in the ground motion to generate large fluctuations in the pore pressure at these low frequencies. This mechanism would have to be frequency dependent, since in the mid-range frequencies (frequencies ranging between 0.195 Hz and 1.563 Hz), the distribution of the square norm ratios for the pore pressure and the acceleration components are of the same order of magnitude.

Considering the mid-range frequencies (frequencies ranging between 0.195 Hz and 1.563 Hz), the acceleration component with the highest correlation with the pore pressure depends on the frequency. In this frequency range, the distribution of the square norm ratios for the pore pressure and the acceleration components take all significant values. The distribution of square norm ratios for the pore pressure has a maximum at 0.391 Hz and decreases rapidly at higher frequencies while the distribution of square norm ratios associated with the acceleration have maxima at larger frequencies of 0.781 Hz or 1.563 Hz. Note that at 1.563 Hz, the correlation between the pore pressure and the three components of the acceleration is close to 0. In other words, the bulk of the distribution of the square norm ratios associated with the acceleration components are out of *frequency phase* with the bulk of the distribution of the square norm of the pore pressure located in the mid-frequency range. Explanation of the distribution of the square norm of the pore pressure as a consequence of the distribution of the square norm-ratios of the acceleration components may require a nonlinear mechanism. This hypothesis will require additional investigations that are beyond the application of the tools discussed in this section.

The correlations between the wavelet coefficients of the pore pressure and the three components of the velocity are shown in Figure 7.8A. The corresponding square norm ratios are in Figure 7.8B. Both the wavelet correlations and the square norm ratios take small values at high frequencies ranging from 3.125 Hz to 100 Hz. At lower frequencies, significant correlation values are observed at 0.024 Hz and 0.048 Hz, but at these frequencies the corresponding values for the square norm ratios are very small for all the seismic signals.

For the mid-range frequencies (frequencies ranging between 0.195 Hz and 1.563 Hz), the vertical velocity component has the highest correlation (in absolute value) with the pore pressure. Over the same range, the distributions of the square norm ratios for the pore pressure and the vertical velocity component have the same functional behavior: they are both described by unimodal functions with maxima at 0.391 Hz and an attenuation at larger frequencies. The vertical component appears to be a good candidate under the assumption of a linear or quasi-linear dependency between the pore pressure and ground velocity. Note that if we consider the frequency range from 0.391 Hz to 1.563 Hz, the results in Figure 7.8 suggest that the EW and NS components of the velocity may also be potential candidates. Over the same frequency range, the correlation between the wavelet coefficients of the EW or NS components and the wavelet coefficients of the pore pressure is smaller in absolute value when compared to the correlation between the vertical component and the pore pressure.

The last data set discussed in this sub-section includes the pore pressure time histories recorded at 3.4 m and the three components of the displacement recorded at 3 m, see Figures 2.3 and 2.4. The correlations between the wavelet coefficients of the pore pressure and the three components of the displacement are shown in Figure 7.9A. The corresponding square norm ratios are in Figure 7.9B. At high and low frequencies, the situation is similar to the situation

involving the pore pressure and the velocity components and will not be discussed further since the same conclusions can be deduced. In the frequency range of interest for the pore pressure, 0.195 Hz to 1.563 Hz, the distributions of the square norm ratio for the displacement is also a unimodal function. Unlike the distribution of the square norm ratio for the pore pressure, the maximum is located at 0.195 Hz. In this frequency range, the wavelet correlation values between the pore pressure and the vertical component of the velocity reported in Figure 7.8A are larger than those reported in Figure 7.9A.

According to the assumption of a linear or quasi-linear dependency between the pore pressure and the ground motion, the most likely candidate to account for the variability of the pore pressure time histories in the frequency range going from 0.195 Hz to 1.563 Hz is the vertical velocity. This result is supported by the first-order model proposed by Mavko and Harp (1984), as well as inferences derived from data analysis discussed in Midoriwaka and Wakamatsu (1988), Kostadinov and Towhata (2002), Wang and Manga (2010). Note that here, the linear or quasi-linear relationship between the pore pressure and the vertical velocity holds only for a finite frequency sub-range of all the frequencies available. Furthermore, contributions from the displacement components or the EW and NS velocity components cannot be disregarded although their contribution should be less important than the contribution due to the vertical velocity. According to the curves shown in Figures 7.7A and 7.7B, small fluctuations in the pore pressure data at high frequencies are likely caused by the vertical component of the acceleration.

7.4 Pore pressure anomaly at low frequencies.

In this sub-section, we discuss the large values of the square norm ratio of the pore pressure observed at low frequencies (see Figure 7.6) and focus on the results obtained at 0.012 Hz. At a frequency of 0.012 Hz, the wavelet coefficients of the three pore pressure signals contribute about 20% of the total signal (see Figure 7.6B). These wavelet coefficients are localized early in the signal (see Figure 5.1) and are well correlated across the “sandy silt to sand” layer (see Figure 7.6A).

When comparing the recorded pore pressure at 3.4 m to ground motion recorded at 3 m at 0.012 Hz frequency, there are no reliable estimates of correlation (as defined in sub-section 6.2) between the wavelet coefficients of the pore pressure and the wavelet coefficients of the ground motion components (see Figure 7.7A to 7.9A) except for the vertical displacement (Figure 7.9A). At this frequency, the square norm ratio of the vertical displacement is close to 0 (Figure 7.9B). Generation of the large fluctuations in the wavelet coefficients of the pore pressure at low frequencies will require a mechanism that locally, in the frequency-time domain, induces a significant amplification of the causal seismic wave that is not observed at other frequencies.

Thus, based on our analysis, *there is no linear or quasi-linear dependency between the pore pressure and the ground motion that can account for the large wavelet coefficients of the pore pressure at low frequencies.* Nonlinear mechanisms and/or geometrical properties specific to the “sandy silt to sand” layer may be responsible for the behaviors observed at the low frequencies. Further investigations are needed to determine if the large values of the square norm ratios of the pore pressure observed at low frequencies can be considered an anomaly.

8. DISCUSSION AND FUTURE DIRECTIONS

In the previous section, we used the wavelet correlation and the square norm ratio to investigate a potential linear or quasi-linear dependency between the pore pressure and the ground motion components in the frequency-time domain. The discussion in the previous section shows that the wavelet correlation and square norm ratio are mutually complementary. Extraction of qualitative and quantitative information about common features between the pore pressure and the ground motion components is simplified when compared to a similar task using traditional tools such as the cross-spectrum (see Section 3).

Although the method discussed in Sub-section 6.2 provides some basis to assess the reliability of the wavelet correlation, the procedure discussed in Section 6 and the results presented in Section 7 are not without limitations. The analysis and the results are based on a wavelet decomposition computed with the Haar basis. In principle, other orthogonal wavelet bases can be considered for analysis: Daubechies wavelet of order n (n integer larger than 0), Coiflet wavelet of order n (n integer with $1 \leq n \leq 5$), and Symlet wavelet of order n (n integer larger than 0). Choosing the wavelet family is not an easy task and trying all, or a significant number of, the available wavelet bases can be a rather cumbersome and time-consuming investigation. This task can be simplified by adopting some criteria to select the wavelet basis. One criterion discussed in the literature consists of selecting the wavelet family by optimizing an entropy measure such as the Shannon entropy discussed in Addison (2002). The basic idea of this procedure is to select a wavelet decomposition with a minimal number of non-zero wavelet coefficients. A small number of wavelet coefficients accounts for all the variability embedded in the signals.

A direct extension to the results reported in Section 7 will consist of computing the lagged wavelet correlations of the seismic signals. Applications of lagged wavelet correlation are discussed in Wilkinson and Cox (1996), van Milligen (1999), and van den Berg (1999). The lag in the time domain will add a third dimension to the correlation analysis. This third dimension may provide a means to quantify features shared by a pair of signals but delayed in time. These features may be scale or frequency dependent and thus best quantified by using wavelet decomposition. Note that these computations can only be performed on wavelet coefficients in the mid-range or high frequency intervals to insure that the number of wavelet coefficients is large enough to compute the lagged cross-correlation at the corresponding scale (for examples see Wilkinson and Cox, 1996).

Analysis up to now has focused on quantifying common features in two different signals as a function of scale or frequency. The quantification is based on computing the correlation or the lagged cross-correlation. Computing only the correlation will miss some of the key features relating the two signals. For instance, describing the relative occurrence of large values in the pore pressure time histories and how they compare to the relative occurrence of large values in the ground motion time histories requires further analysis. Computations of the distributions, or of distribution-derived parameters, are best estimated for white or quasi-white noise. Figures 3.2 and 3.3 clearly show that the spectra of both the recorded pore pressure and ground motion are frequency dependent. This indicates that each of these time series is auto-correlated, since the spectrum of white noise is flat. One important property of the wavelet transforms is that they tend “to simplify the dependence structure of the original data”, to whiten or decorrelate the original signal (Vidakovic, 1999, p. 18; and references therein). Or, as indicated by Kumar and Foufoula-Georgiou (1997, p. 386), “... although fractional Brownian motion is a nonstationary, and

infinitely correlated process, its wavelet coefficients are stationary and practically uncorrelated.” As a first step, deciphering the distributions of the wavelet coefficients of the pore pressure and the ground motion will require the computation of the skewness factor and flatness factor of their respective wavelet coefficients as a function of the scale or the frequency (Meneveau, 1991; Schneider and Farge, 2001; Addison, 2002). The skewness factor and flatness factor are used in the study of turbulent flow to determine deviation of the distribution of the wavelet coefficients from a Normal distribution. If the estimate of these factors shows that the wavelet coefficients are not distributed according to a Normal distribution, a further step will consist in estimating the distribution of the wavelet coefficients at different scales and matching the computed distributions with theoretical probability laws. Of particular interest will be to compare with probability laws used to describe the distribution of peak ground acceleration (PGA) and peak ground velocity (PGV), see Abrahamson (1988), Gusev (1989; 1996), Lavallée and Archuleta (2005), Lavallée (2008), Yamada *et al.* (2009), Huyse *et al.* (2010), and Lavallée *et al.* (2011).

9. CONCLUSION

The 2011 Tohoku-oki –officially renamed Higashi Nihon Daishinsai- (Japan) is the most recent example of liquefaction resulting from earthquake induced pore pressure fluctuation. Liquefaction is a common result of earthquakes and capable of causing considerable damage (e.g., Seed and Idriss, 1971; Wang and Manga, 2010). The causative mechanism responsible for liquefaction is closely related to earthquake excitation. Currently, there are very few sites that are equipped with instruments to monitor simultaneously both pore pressure and ground motion. In view of mitigating the hazard associated with liquefaction, it is imperative to understand the complex relationship between pore pressure data and ground motion (see Wang and Manga, 2010). Such relations can be applied to sites and areas where there is no record of excess pore pressure, but where ground motion data are available to complement the design of liquefaction probability curves (Holzer *et al.*, 2009 and references therein).

In this paper, we discussed tools that can provide insights about the complex relationship between pore pressure data and ground motion. The tools are based on wavelet decomposition. Wavelet-derived tools are designed to properly analyze signals with an intermittent frequency content (see Figures 2.3 and 2.4). The tools consist in computing the wavelet correlation and the square norm ratio of the two signals under investigation. Wavelet correlation quantifies the degree of linear or quasi-linear dependence between the two signal wavelet coefficients as a function of the frequency. The square norm ratios complement the information provided by the wavelet correlation by weighting the relative contribution of the wavelet coefficients to the signals as a function of the frequency. In Section 7, we discussed the computations of the wavelet correlation and the square norm ratios for different sets of two seismic signals. In this paper, we considered pore pressure time histories and acceleration time histories recorded at the USGS Wildlife station during the 2010 Sierra el Mayor-Cucapah earthquake.

A first significant result is obtained by computing the correlation of the wavelet coefficients associated with the horizontal components of the acceleration recorded at different depths. The curve of the wavelet correlation as a function of the frequency shows a sudden jump in the high frequency range. The jump can be explained in terms of independent measurements of the shear wave velocity. Furthermore, this result can be understood as a validation of the wavelet-derived tools used in this paper. Another significant result discussed in Section 7 is the

observation of a range of frequencies where wavelet coefficients of pore pressure are relatively well correlated to the wavelet coefficients of the vertical component of the velocity, while the estimated square norm ratios of both wavelet coefficients follow a similar unimodal curve with maxima located at the same frequencies. This finding may provide a basis for quantifying and modeling the complex relationship between the pore pressure and the ground motion in the frequency-time domain.

The tools discussed in this paper may also be helpful in addressing another question. In the book “Quantitative Seismic Interpretation” by Avseth *et al.* (2005, p. 42), the authors write “Cuttings, cores, and logs tell us about the lithology, porosity, permeability, and fluids. And assuming that there is a good tie between seismic and synthetics, we may even say that we understand the seismic data at the well. The problem is, often, knowing what happens when moving away from the well.” Answering this question is fundamental when comparing time series recorded by portable stations to time series recorded by *in situ* stations (Cochran *et al.*, 2011). It is also fundamental for the dissemination of current and next generation seismic instrumentation, including borehole instrumentation. Understanding spatial variations of ground motion is important in both seismology and earthquake engineering (Kramer, 1996; and Field and Hough, 1997). In Section 7.1 and 7.2, we provide some answers to the question raised by Avseth *et al.* (2005, p. 42). The procedure discussed in this paper can be used to compare seismic signals recorded at different locations, or at different depths, with similar geological environments and to quantify the common features shared by the seismic signals as a function of frequency. Boreholes are drilled and instrumented to provide direct measurements of ground motion during an earthquake. These recorded ground motions are the basis for predicting ground shaking at other locations with similar geological settings. Our tools will be useful to improve the reliability of those predictions.

10. ACKNOWLEDGEMENTS

The authors would like to thank Hank Ratzesberger for initiating this investigation of the seismic signals recorded during the 2010 Sierra el Mayor-Cucapah earthquake and Paul Hegarty for his engineering expertise. This research was supported by the Earthquake Hazards Program of the United States Geological Survey. The [NEES@UCSB](#) site is funded in part by the George E. Brown, Jr. Network for Earthquake Engineering Simulation ([NEES](#)) Program of the National Earthquake Hazards Reduction Program ([NEHRP](#)) of the National Science Foundation ([NSF](#)) under Award Number **CMMI-0927178**.

11. BIBLIOGRAPHY OF ALL PUBLICATIONS RESULTING FROM THE WORK PERFORMED UNDER THE AWARD

Coupling of Pore Pressure and Ground Motion Data Recorded During the 2010 El Mayor-Cucapah (Baja California) Earthquake at the NEES@UCSB Wildlife Station. Seale, S. W. H., Lavallee, D., Steidl, J. H., Hegarty, P., *Seismological Research Letters*, 83:2, Pg. 398, 2012.

Coupling of Pore Pressure and Ground Motion: Further Studies Using Data Recorded at the NEES@UCSB Wildlife Station, Abstract NH31C-1635, Seale, Sandra H., Lavallee, Daniel, Archuleta, Ralph, Steidl, Jamison, presented at 2012 Fall Meeting, AGU, San Francisco, Calif., 3-7 Dec.

12. REFERENCES

- Abrahamson, N. A. (1988), Statistical properties of peak ground accelerations recorded by the SMART 1 array, *Bull. Seismol. Soc. Am.*, **78**, 26-41.
- Adamowski, J. F. River flow forecasting using wavelet and cross-wavelet transform models. *Hydrol. Process.* **22**, 4877–4891, 2008
- Addison, P. S., K. B. Murray, and J. N. Watson. Wavelet transform analysis of open channel wake flows. *ASCE J. Engng Mech.* **127**, 59-70, 2001.
- Addison, P. S. The illustrated wavelet transform handbook. Institute of Physics Publishing, Bristol. 353pp., 2002
- Avseth, P., T. Mujerki, and G Mavko. Quantitative seismic interpretation. Cambridge University Press. 359pp., 2005.
- Baker, J. W. Quantitative Classification of Near-Fault Ground Motions Using Wavelet Analysis. *Bull. Seis. Soc. Am.*, **97**, doi: 10.1785/0120060255, 1486-1501, 2007.
- Bonilla, L. F., R. J. Archuleta,, and D. Lavallée. Hysteretic and Dilatant Behavior of Cohesionless Soils and their Effects on Nonlinear Site Response: Field Data Observations and Modeling. *Bull. Seism Soc. Am.*, **95**, doi: 10.1785/0120040128, 2373–2395, 2005.
- Bruce, L. M., C. F. Koger, and J. Li. Dimensionality Reduction of Hyperspectral Data Using Discrete Wavelet Transform Feature Extraction. *IEEE Trans. Geosci. Remote Sens.*, **40**, 2331-2338, 2002.
- Chui, C. K. An introduction to wavelets. Academic press, San Diego. 264pp., 1992.
- Cochran, E. S., J. F. Lawrence, A. Kaiser, B. Fry, and A. Chung. Comparison between low-cost and traditional MEMS accelerometers: A case study from the M7.1 Darfield, New Zealand Aftershock deployment. *Annals of Geophysics*, **54**, 6, doi: 10.4401/ag-5268, 2011.
- Collineau, S., and Y. Brunet, Detection of turbulent coherent motions in a forest canopy, Part I, Wavelet analysis. *Boundary Layer Meteorol.*, **65**, 357-379, 1993.
- Daubechies, I. and W. Sweldens. Factoring wavelet transforms into lifting steps. *J. Fourier Anal. Appl.*, **4**, 245-267, 1998
- D’Auria, L., F. Giudicepietro, M. Martini, M. Orazi, R. Peluso, and G. Scarpato, Polarization Analysis in the Discrete Wavelet Domain: An Application to Volcano Seismology. *Bull. Seis. Soc. Am.*, **100**, doi: 10.1785/0120090166, 670-683, 2010.
- Field, E. H. and S. E. Hough. The variability of PSV response spectra across a dense array deployed during the Northridge aftershock sequence, *Earthq. Spectra*, **13** (2), 243-257, 1997.
- Frankel, A. D., D. L. Carver, and R. A. Williams. Nonlinear and Linear Site Response and Basin Effects in Seattle for the M 6.8 Nisqually, Washington, Earthquake. *Bull. Seismol. Soc. Am.*, **92**, 2090-2109, 2002.
- Goumas, S. K., M. E. Zervakis, and G. S. Stavrakakis. Classification of Washing Machines Vibration Signals Using Discrete Wavelet Analysis for Feature Extraction, *IEEE Transaction on instrumentation and measurement*, **51** (3), 497-508, 2002.
- Gurley, K., and, A. Kareem. Applications of wavelet transforms in earthquake, wind, and ocean engineering. *Eng. Struct.*, **21**, 149–167. 1999.

- Gusev, A. A. Multiasperity model fault model and the nature of short-periods subsources. *Pure Appl. Geophys.*, **136**, 515-527, 1989.
- Gusev, A., A. Peak factors of Mexican accelerograms: evidence of a non-Gaussian amplitude distribution. *J. Geophys. Res.*, **101**, 20,083-20,090, 1996.
- Holzer, T. L., T. L. Youd, and T. C. Hanks. Dynamics of liquefaction during 1987 Superstition Hills, California, earthquake, *Science* **244**, 56–59, 1989.
- Holzer, T.L. and T.L. Youd. Liquefaction, ground oscillation, and soil deformation at the Wildlife Array, California, *Bull. Seis. Soc. Am.*, **97**, 961–976, 2007.
- Holzer, T.L., T. E. Nölce and M. J. Bennett. Scenario Liquefaction Hazard Maps of Santa Clara Valley, Northern California. *Bull. Seis. Soc. Am.*, **97**, doi: 10.1785/0120080227, 367-381, 2009.
- Huyse, L., R. Chen, and J. A. Stamatakis Application of Generalized Pareto Distribution to Constrain Uncertainty in Peak Ground Accelerations. *Bull. Seismol. Soc. Am.*, **100**, doi: 10.1785/0120080265, 87–101, 2010.
- Iai, S., T. Morita, T. Kameoka, Y. Matsunaga, and K. Abik. Response of a dense sand deposit during 1993 Kushiro-Oki Earthquake, *Soils Found.* **35**, 115–131, 1995.
- Jensen, A. and A. la Cour-Harbo. *Ripples in mathematic*. Springer, Berlin. 246pp., 2001.
- Katul G. G., M. B. Parlange, and C. R. Chu. Intermittency, local isotropy, and non-Gaussian statistics in atmospheric layer turbulence. *Phys. Fluids*, **6** (7), 2480-2492, 1994
- Katul, G. G. and, M. B. Parlange. Analysis of land surface heat fluxes using the orthonormal wavelet approach. *Water Resour. Res.* **31**, 2743–2749. 1995.
- Kulkarni, J. R., L. K. Sadani, and, B. S. Murthy. Wavelet analysis of intermittent turbulent transport in the atmospheric surface layer over a monsoon trough region. *Boundary-Layer Meteorol.*, **90**, 217–239, 1999.
- Kostadinov, M.V., and I. Towhata. Assessment of liquefaction-inducing peak ground velocity and frequency of horizontal ground shaking at onset of phenomenon, *Soil Dyn. Earthq. Eng.*, **22**, 309–322, 2002.
- Kramer, S. L. *Geotechnical Earthquake Engineering*, Prentice Hall, New Jersey, 653 pp, 1996.
- Kumar, P., and E. Foufoula-Georgiou. Wavelet analysis for geophysical applications, *Rev. Geophys.*, **85**, no. 4, 385–412, 1997.
- Lavallée, D., and R. J. Archuleta. Coupling of the random properties of the source and the ground motion for the 1999 Chi Chi earthquake, *Geophys. Res. Lett.*, **32**, L08311, doi:10.1029/2004GL022202, 2005.
- Lavallée, D. On the Random Nature of Earthquake Sources and Ground Motions: A Unified Theory. In *Earth Heterogeneity and Scattering Effects in Seismic waves*, edited by R. Dmowska, H. Sato and M. Fehler, *Advances in Geophysics*, **50**. 427-461, 2008.
- Lavallée, D., H. Miyake and K. Koketsu. Stochastic Model of a Subduction-Zone Earthquake: Sources and Ground Motions for the 2003 Tokachi-oki, Japan, Earthquake. To be published in *Bull. Seism Soc. Am.*, 2011.
- Lindsay, R. W., D. B. Percival, and D. A. Rothrock. The discrete wavelet transform and the scale analysis of the surface properties of sea ice. *IEEE Trans. Geosci. Remote Sens.*, **34**, 771–787. 1996
- Liu, P. C., 1994: Wavelet spectrum analysis and ocean wind waves. *Wavelets in Geophysics*, E. Foufoula-Georgiou and P. Kumar, Eds., Academic Press, 151–166.
- Mallat, S. *A wavelet tour of signal processing*. Academic press, San Diego. 637pp., 1998.

- Mavko, G. M., and E. Harp. Analysis of wave-induced pore pressure changes recorded during the 1980 Mammoth Lakes, California, earthquake sequence. *Bull. Seismol. Soc. Am.*, **74**, 1395-1407, 1984.
- Meneveau, C. Analysis of turbulence in the orthonormal wavelet representation. *J. Fluid Mech.*, **232**, 469-520, 1991.
- Meyers, S. D., B. G. Kelly, and J. J. O'Brien. An introduction to wavelet analysis in oceanography and meteorology: With application to the dispersion of Yanai waves. *Mon. Wea. Rev.*, **121**, 2858-2866, 1993.
- Midorikawa, S., and K. Wakamatsu. Intensity of earthquake ground motion at liquefied sites, *Soils Found.*, **28**, 73-84, 1988.
- van Milligen, B. P. Wavelet, non-linearity and turbulence in plasmas. *In Wavelet in Physics*. Edited by J. C. van den Berg, □Cambridge University, New York. 227-262, 1999.
- Misiti, M., Y. Misiti, G. Oppenheim and J.-M. Poggi. Wavelets and Their Applications. ISTE. 330 pp, 2007.
- Ogden, R. T., Essential Wavelets for Statistical Applications and Data Analysis, Birkhäuser, Boston. 206pp., 1997.
- Papanicolaou, G. C. and K. Solna, Wavelet Based Estimation of Local Kolmogorov Turbulence. *In Theory and applications of long-range dependence*. Edited by P. Doukhan, G. Oppenheim, and M. S. Taqqu. Birkhäuser, Boston. 473-505, 2003.
- Papoulis, A. Probability. Random Variables, and Stochastic Processes. McGraw-Hill, New York. 666pp, 1991.
- Percival, D., A. Walden. Wavelets Methods for Time Series Analysis. Cambridge University. 594pp, 2000.
- Riera-Guas, M., J. A. Antonino-Daviu, M. Pineda-Sanchez, R. Puche-Panadero, and J. Perez-Cruz. A General Approach for the Transient Detection of Slip-Dependent Fault Components Based on the Discrete Wavelet Transform. *IEEE Trans. Ind. Electron.*, **55**, 4167-4180, 2008.
- Schneider, K., and M. Farge. Computing and analyzing turbulent flow using wavelets. *In Wavelet transforms and time-frequency signal analysis*. Edited by L. debnath. Birkhäuser, Boston. 182-216, 2001.
- Seed, H. B., and I. M. Idriss. Simplified procedure for evaluating soil liquefaction potential, *J. Soil Mech. Found. Div.*, **97**, 1249-1273, 1971.
- Smith, L. C., D. L. Turcotte and B. L. Isacks. Stream flow characterization and feature detection using a discrete wavelet transform. *Hydrological Process*, **12**, 233-249, 1998.
- Steidl, J. H. and S. Seale. Observations and analysis of ground motion and pore pressure at the NEES instrumented geotechnical field sites. *Proceedings of the 5th International Conference on Recent Advances in Geotechnical Earthquake Engineering and Soil Dynamics, San Diego, CA*. Paper No. 133b, ISBN-887009-15-9, May 24-29, 2010.
- Sornette, D. Critical phenomena in natural sciences. Springer, Berlin. 528pp., 2004.
- Sweldens, W. The Lifting Scheme: A Construction of Second Generation Wavelets. *Siam J. Math. Anal.*, **29**, 511-546, 1997.
- Tibuleac, I. M. and E. T. Herrin. An Automatic method for determination of L_g arrival times using wavelet methods, *Seism. Res. Lett.*, **70**, 577-595, 1999.
- Tibuleac, I. M., E. T. Herrin, J. M. Britton, R. Shumway and A. C. Rosca.. Automatic determination of secondary seismic phase arrival times using wavelet transform, *Seism. Res. Lett.*, **74**, 884-892, 2003.

- Torrence C, and G. Compo. A practical guide to wavelet analysis. *Bulletin of the American Meteorological Society* **79**: 61–78, 1998.
- Unser, M. Texture Classification and Segmentation Using Wavelet Frames. *IEEE Trans. Image Processing* , **4**, 1549-1560, 1995.
- Vidakovic, B. Statistical modeling by wavelets. John Wiley & Sons, New York. 382pp., 1999.
- Wang, C.-Y., A. Wong, D.S. Dreger, and M. Manga. Liquefaction limit during earthquakes and underground explosions – implications on ground-motion attenuation, *Bull. Seis. Soc. Am.*, **96**, 355–363, 2006.
- Wang, C.-Y. Liquefaction beyond the near field, *Seismo. Res. Lett.*, **78**, 512–517, 2007.
- Wang, C.-Y., and M. Manga. Earthquake and water. Springer-verlag, Berlin, 225pp., 2010.
- Wong, A., and C.-Y. Wang Field relations between the spectral composition of ground motion and hydrological effects during the 1999 Chi-Chi (Taiwan) earthquake. *J. Geophys. Res.*, **112**, B10305, doi:10.1029/2006JB004516, 2007.
- Wilkinson, W. A., and M. D. Cox, “Discrete wavelet analysis of power system Transients,” *IEEE Trans. Power Syst.*, **11**, 2038–2044, 1996.
- Yamada, M., A. H. Olsen, and T. H. Heaton. Statistical Features of Short-Period and Long-Period Near-Source Ground Motions. *Bull. Seismol. Soc. Am.*, **99**, doi: 10.1785/0120090067, 3264–3274, 2009.
- Youd T. L., J. H. Steidl, and R. L. Nigborc. Lessons learned and need for instrumented liquefaction sites. *Soil Dynamics and Earthquake Engineering*, **24**, 639–646, 2004.
- Zeghal, M., and A.-W. Elgamal. Analysis of site liquefaction using earthquake records, *J. Geotech. Eng.* **120**, 996–1017, 1994.